Element Array by Scanning X-ray Fluorescence Microscopy after *Cis*-Diamminedichloro-Platinum(II) Treatment

Mari Shimura,[1] Akira Saito,[4,8,9] Satoshi Matsuyama,[5] Takahiro Sakuma,[1] Yasuhito Terui,[3] Kazumasa Ueno,[5] Hirokatsu Yumoto,[5] Kazuto Yamauchi,[5] Kazuya Yamamura,[6] Hidekazu Mimura,[5] Yasuhisa Sano,[5] Makina Yabashi,[7] Kenji Tamasaku,[8] Kazuto Nishio,[2] Yoshinori Nishino,[8] Katsuyoshi Endo,[6] Kiyohiko Hatake,[3] Yuzo Mori,[6] Yukihito Ishizaka,[1] and Tetsuya Ishikawa[8]

[1]Department of Intractable Diseases, International Medical Center of Japan; [2]Pharmacology Division, National Cancer Center Research Institute; [3]Division of Clinical Chemotherapy, Cancer Chemotherapy Center, Japanese Foundation for Cancer Research, Tokyo, Japan; Departments of [4]Material and Life Science and [5]Precision Science and Technology, and [6]Research Center for Ultra-Precision Science and Technology, Graduate School of Engineering, Osaka University, Suita, Osaka, Japan; [7]SPring-8/Japan Synchrotron Radiation Research Institute and [8]SPring-8/Riken, Hyogo, Japan; and [9]Nanoscale Quantum Conductor Array Project, ICORP, Saitama, Japan

Abstract

Minerals are important for cellular functions, such as transcription and enzyme activity, and are also involved in the metabolism of anticancer chemotherapeutic compounds. Profiling of intracellular elements in individual cells could help in understanding the mechanism of drug resistance in tumors and possibly provide a new strategy of anticancer chemotherapy. Using a recently developed technique of scanning X-ray fluorescence microscopy (SXFM), we analyzed intracellular elements after treatment with *cis*-diamminedichloro-platinum(II) (CDDP), a platinum-based anticancer agent. The images obtained by SXFM (element array) revealed that the average Pt content of CDDP-resistant cells was 2.6 times less than that of sensitive cells, and the zinc content was inversely correlated with the intracellular Pt content. Data suggested that Zn-related detoxification is responsible for resistance to CDDP. Of Zn-related excretion factors, glutathione was highly correlated with the amount of Zn. The combined treatment of CDDP and a Zn(II) chelator resulted in the incorporation of thrice more Pt with the concomitant down-regulation of glutathione. We propose that the generation of an element array by SXFM opens up new avenues in cancer biology and treatment. (Cancer Res 2005; 65(12): 4998-5002)

Introduction

Cis-Diamminedichloro-platinum(II) (CDDP) is an effective anticancer agent, but tumor cells can become resistant after CDDP-based therapy (1). Detoxification of CDDP, an increase in DNA repair, and excretion of CDDP have been implicated as major factors contributing to CDDP resistance (1). Incorporated CDDP is excreted by several molecules, such as overexpressed P-glycoprotein (2), a zinc-related defense system that is regulated by increased intracellular glutathione (GSH; ref. 3), and the ATP-dependent glutathione S-conjugate export pump (GS-X pump), which plays a role in the vesicle-mediated excretion of GSH-CDDP conjugates from resistant cells (4). Recent reports suggest

that minerals such as zinc (Zn) and copper (Cu), important for normal cellular functions (5), are involved in CDDP resistance (6, 7). The simultaneous monitoring of multiple numbers of cellular elements would be helpful in identifying the mechanism of drug resistance in a malignant cell. The recently developed technique of scanning X-ray fluorescence microscopy (SXFM; refs. 8, 9) has made it possible to detect elements of interest by a single measurement and give a profile of these elements at the single-cell level (termed an element array). To examine the efficacy of element array analysis, we analyzed elements before and after treatment with CDDP and compared the element profiles of CDDP-sensitive and CDDP-resistant cells. We showed that the Zn content has an inverse correlation with Pt incorporation owing to a positive linkage with glutathione (GSH), a Zn-dependent detoxification factor. The combined treatment with CDDP and *N*,*N*,*N*,*N*-tetrakis-(2-pyridylmethyl)-ethylenediamine (TPEN), a Zn (II)-chelator (10), increased Pt uptake with a concomitant reduction of intracellular GSH. We propose that the element array is a versatile method suitable for obtaining information about metals involved in drug metabolism and could contribute to a novel strategy for anticancer chemotherapy.

Materials and Methods

Element array analysis by scanning X-ray fluorescence microscopy. SXFM was set up at an undulator beamline, BL29XU, of the SPring-8 synchrotron radiation facility (11) by combining a Kirkpatrick-Baez–type X-ray focusing system (12, 13), an XY-scanning stage for sample mounting, and an energy-dispersive X-ray detector (SDD, Röntec. Co., Ltd.). Monochromatic X-rays at 15 keV for Pt *L*-line excitation were focused into a 1.5 μm (*H*) × 0.75 μm (*W*) spot with a measured flux of ~1×10^{11} photons/s. The focused X-rays simultaneously yielded the fluorescence of various chemical species in a small volume of sample cells, as shown in Fig. 1*A*. The fluorescence from each element was taken independently and did not overlap except for the Pt*Lα* signal, which was contaminated by Zn*Kβ* (Fig. 1*A*). This was corrected by subtraction, as described previously (8). In this study, we could also measure Pt*Lβ* as a unique signal of Pt (Fig. 1*A*). After counts were collected for 4.0 to 8.5 seconds at each pixel of scanning, the detected counts were normalized by incident beam intensity. In addition to the mapping images, an elemental concentration per single cell was calculated from the integrated elemental intensity over the whole mapping image.[10]

Requests for reprints: Yukihito Ishizaka, Department of Intractable Diseases, International Medical Center of Japan, 1-21-1 Toyama, Shinjuku-ku, 162-8655 Tokyo, Japan. Phone/Fax: 81-3-5272-7527; E-mail: zakay@ri.imcj.go.jp.

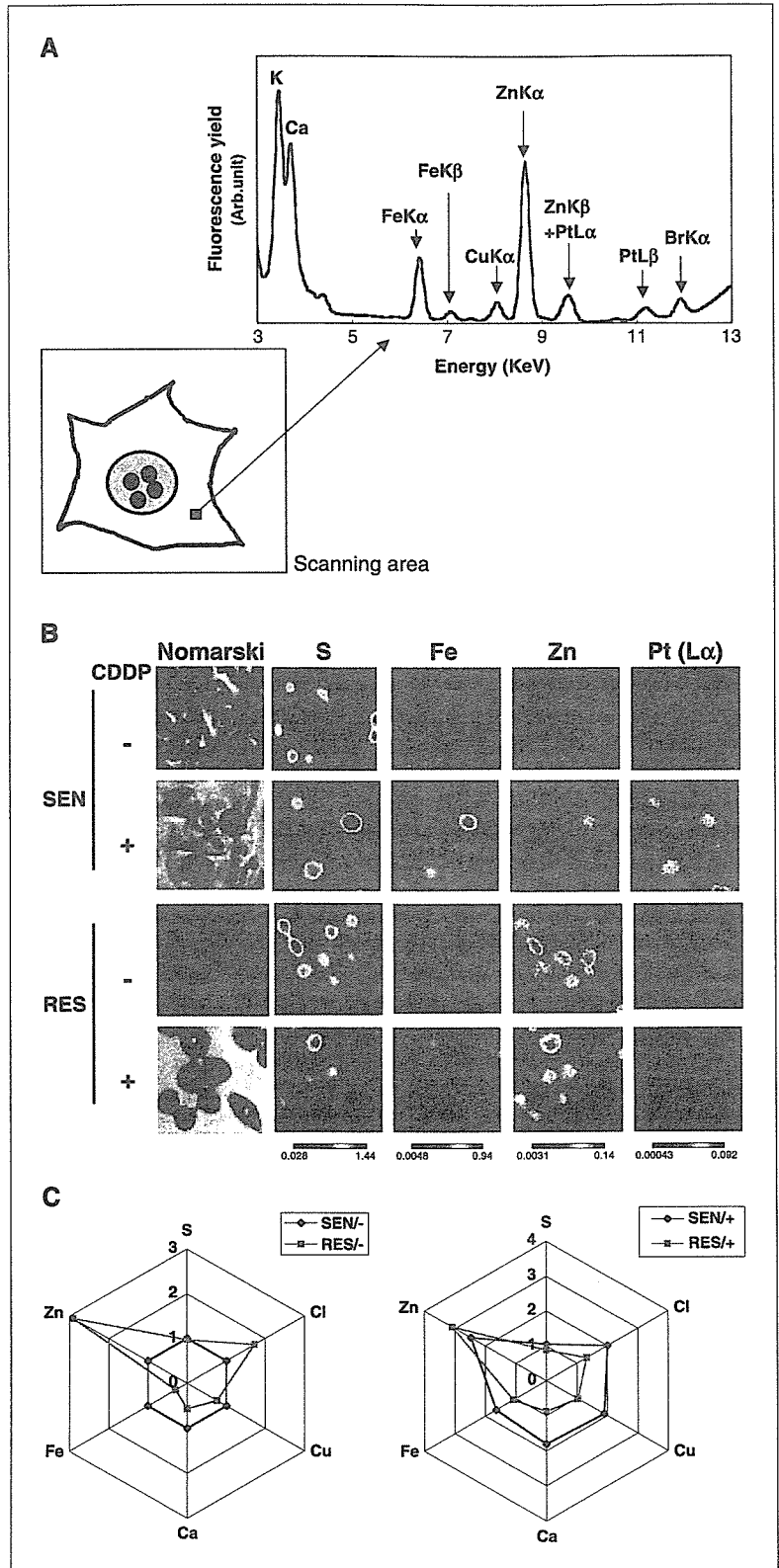[10] A. Saito et al., manuscript in preparation.

— 39 —

Figure 1. Element array by SXFM. *A*, scheme of imaging cellular elements by SXFM. Coherent X-rays are focused on each area (*pixel*), and the X-ray fluorescence from each element is detected. Each pixel gives an elemental spectrum, as shown in the right panel, and an integrated intensity of the individual element was mapped to the corresponding area of analyzed cells. *B*, SXFM analysis after CDDP treatment. Cell morphologies obtained by Nomarski are shown at ×100 magnification (*left*). Each field of view is equivalent to an area of 70 × 70 μm. Representative results are shown. Brighter colors indicate a higher signal intensity of each element. Results are shown for PC/SEN (*top*) and PC/RES cells (*bottom*). Note the high intensity of PtLα in PC/SEN cells after CDDP treatment (*second panel of the Pt column*) and the higher signal intensity of Zn in PC/RES cells compared with that of PC/SEN cells. *C*, element array based on SXFM analysis. The mean signal intensity of each element obtained by SXFM analysis was calculated, and the fold increase of elements in PC/RES cells (*red*) was depicted by using the intensity in PC/SEN cells (*blue*) as a standard (*left*). A part of analyzed elements is shown. The fold increase of elements in PC/SEN (*blue*) and PC/RES cells (*red*) after CDDP treatment was also shown by using the intensity in PC/SEN before CDDP treatment as a standard (*right*).

Chemicals and biochemical assays. TPEN (Sigma, St. Louis, MO; ref. 10), GSH (Calbiochem, La Jolla, CA), and CDDP (Daiichi Kagaku, Tokyo, Japan) were purchased. A GSH colorimetric assay kit (Calbiochem) and a BCA protein assay kit (Bio-Rad, Hercules, CA) were used for measuring

intracellular GSH. About 3×10^5 to 4×10^5 cells were subjected to GSH measurement, and the data were normalized by cell number.

Cell lines. PC-9 cells (PC/SEN) and PC-9 cells resistant to CDDP (PC/RES), originally derived from a lung carcinoma cell line (14), were

maintained in DMEM (Nissui, Co., Tokyo, Japan) supplemented with 10% FCS (Sigma). The viability of PC/SEN cultured for 72 hours in the presence of 1 μmol/L CDDP was 40%, whereas that of PC/RES was ~90%. In this study, each cell line when treated with 1 μmol/L CDDP for 24 hours showed >85% viability.

Colony formation. After treatment, aliquots of PC/SEN and PC/RES were plated into culture dishes or soft agar, and the numbers of cell aggregates consisting of >50 cells were counted. Each number was normalized by plating efficiency, and the mean and SD of the number of formed colonies were calculated.

Sample preparation. Cells were plated on a silicon nitride base (NTT Advanced Technology, Tokyo, Japan) 1 day before the experiment. After incubation for 24 hours in the presence of 1 μmol/L CDDP, the cells were washed with PBS, fixed in 2% paraformaldehyde in PBS for 10 minutes at room temperature, and incubated in cold 70% ethanol for 30 minutes. The cells were then placed in a 1:3 solution of glacial acetic acid and methanol for 10 minutes, washed with 70% alcohol, and dried overnight at room temperature.

Measurement of cellular platinum and zinc. To measure Pt and Zn, ~5 × 10^6 cells were subjected to inductively coupled plasma mass spectroscopy (ICP-MS; Toray Research Center, Shiga, Japan; ref. 15).

Statistical analysis. The Pearson product-moment correlation coefficient and Student's t test were used to evaluate statistical significance (16).

Results and Discussion

Incorporation of platinum and element array after *cis*-diamminedichloro-platinum(II) treatment. We analyzed intracellular elements by SXFM after CDDP treatment (Fig. 1A). At 12 hours after treatment with 1 μmol/L CDDP, the level of Pt was increased in PC/SEN cells, whereas little increase in the Pt level was seen in PC/RES cells (Fig. 1B). The intensity of Pt in PC/RES cells was 2.6-fold less than that in PC/SEN cells, as confirmed by the results of ICP-MS, which indicated that the amount of Pt in PC/RES cells (5.5 fg/cell) was 3.6-fold less than that in PC/SEN cells (19.7 fg/cell). Therefore, the decreased accumulation of CDDP is likely to be responsible for resistance in PC/RES cells.

Based on the mean signal intensity obtained by SXFM, element array analysis was carried out (Fig. 1C). The element profile
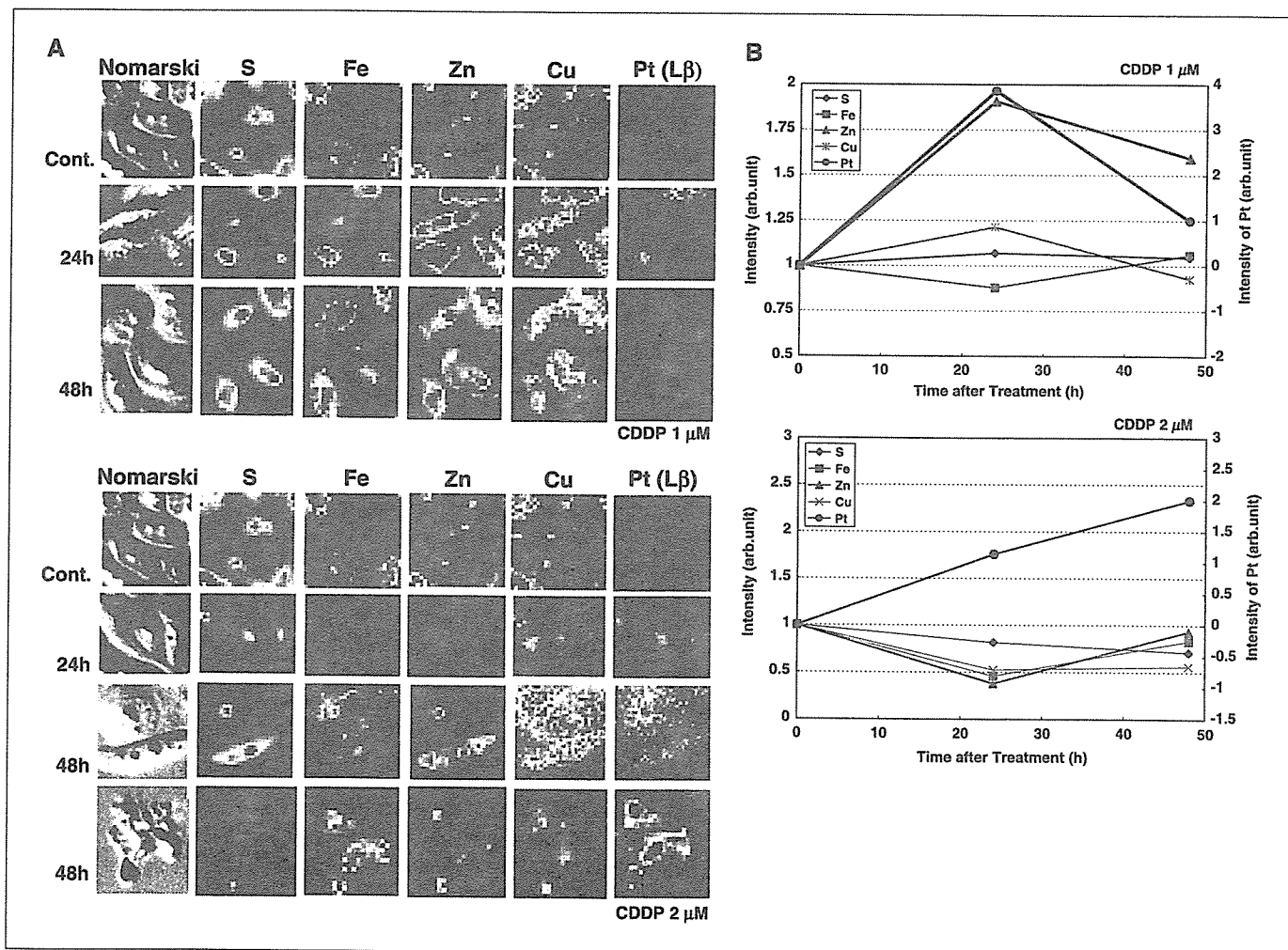

Figure 2. Chronological changes in elements after CDDP treatment. *A,* detection of elements in CDDP-treated PC/SEN cells. From the left, Nomarski images, signals of S, Fe, Zn, Cu, and Pt are shown. Top and bottom sets of panels show cells treated with 1 and 2 μmol/L CDDP, respectively. In each set of panels, control cells (*top*) and cells treated with CDDP for 24 hours (*middle*) and 48 hours (*bottom*) are shown. In this experiment, the signals of PtLβ were measured instead of PtLα (see Materials and Methods). The lowest panels show an apoptotic cell after 48 hours. *B,* summarized results of chronological changes of elements. The results after treatment with 1 μmol/L (*top*) and 2 μmol/L CDDP (*bottom*) are shown. The mean signal intensity was calculated from the results partly shown in (*A*). Among the cellular elements, Zn was most influenced by both 1 and 2 μmol/L CDDP treatment and had an inverse correlation with Pt content.
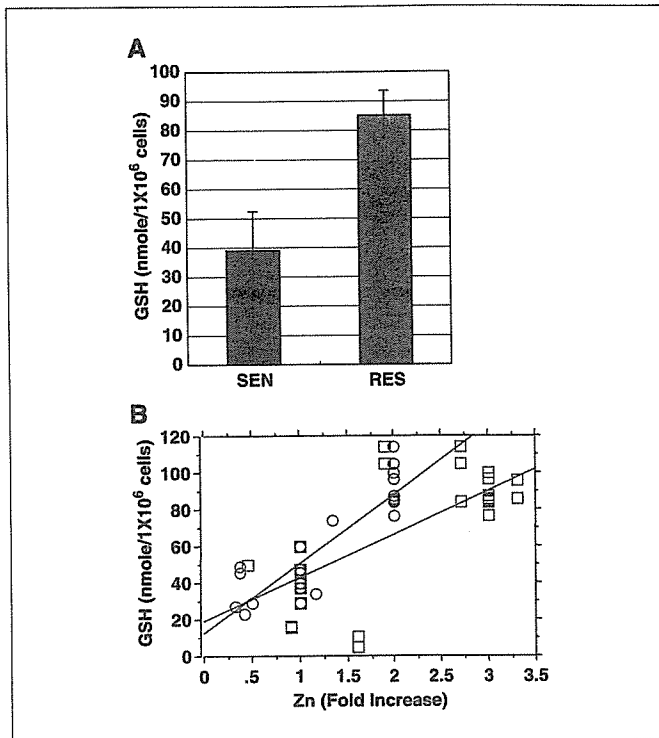
— 41 —

Figure 3. Cellular Zn content and GSH. *A,* basal level of intracellular GSH. The intracellular GSH levels in PC/SEN (*black*) and PC/RES cells (*gray*) were measured. GSH was significantly higher in PC/RES than in PC/SEN cells (*t* test, $P < 0.05$). *B,* correlation between Zn and intracellular GSH. A scatter diagram for Pearson product-moment correlation coefficient is depicted. Zn, measured by SXFM (*red squares, n = 27*) and by ICP-MS (*green circles, n = 29*), was plotted against intracellular GSH. Scattered values were based on data from both PC/SEN and PC/RES cells. The correlation coefficient *r* was calculated, and the statistical significance was determined ($P < 0.05$).

facilitates the identification of the elements related to the mechanism of drug resistance to CDDP. First, we noticed that the Zn content of untreated PC/RES cells was ~3-fold of that in PC/SEN cells (Fig. 1*C, left*). The difference in the Zn contents of these cells was confirmed by ICP-MS analysis (105 fg/cell for PC/SEN cells and 189 fg/cell for PC/RES cells, respectively). When 1 μmol/L CDDP was used for treatment, constitutive high Zn was observed in PC/RES (Fig. 1*C, right*). In PC/SEN cells, the amounts of all the elements were slightly increased, but the amount of Zn was increased most markedly.

We then analyzed the chronological changes in the levels of elements in PC/SEN cells following CDDP treatment. Representative results for S, Fe, Zn, Cu, and Pt are shown in Fig. 2*A*. Pt was clearly observed at 24 hours after treatment with 1 or 2 μmol/L CDDP (Fig. 2*A*). It was, however, barely detectable at 48 hours after the cells were treated with 1 μmol/L CDDP (Fig. 2*A, top*), suggesting that the cells excreted CDDP. In contrast, the cellular content of Pt gradually increased after treatment with 2 μmol/L CDDP (Fig. 2*A, bottom*), and apoptotic cells with high levels of incorporated CDDP were observed after 48 hours (Fig. 2*A, bottom*).

The element profile was plotted against the time after treatment with CDDP (Fig. 2*B*). When the cells were treated with 1 μmol/L CDDP, the Zn content increased remarkably and reached a peak at 24 hours (Fig. 2*B, top, red line*). In these cells, the Pt content was reduced after 48 hours. When the cells were treated with 2 μmol/L CDDP, the Zn content decreased within 24 hours (Fig. 2*B, bottom*),

and the Pt content increased within 48 hours. In this analysis, Cu did not show significant changes. The results imply that the intracellular Zn content has an inverse correlation with the incorporated Pt content.

Cellular zinc and zinc-related detoxification. We studied Zn-related detoxification factors, such as metallothioneins (17), GSH (18), and the GSH-coupled excretory pump GS-X (4), and we observed that intracellular GSH was high in PC/RES cells (Fig. 3*A*). We then examined the possible correlation between the intracellular Zn content and GSH. As shown in Fig. 3*B*, the GSH levels showed a significant correlation with the levels of Zn detected by both ICP-MS and SXFM (Pearson product-moment correlation coefficient $r = 0.794$, $P < 0.05$ and $r = 0.533$, $P < 0.05$, respectively). The levels of Zn detected by SXFM may have less correlation with GSH than do the levels detected by ICP-MS because SXFM analyzed Zn in a small number of cells, whereas the analyses of GSH using ICP-MS were carried out on >10^5 cells.

Effects of zinc depletion and *cis*-diamminedichloro-platinum(II) uptake. To examine ways of increasing the sensitivity of PC/RES cells to CDDP, we used the Zn(II) chelator TPEN, as it was thought that CDDP uptake would increase when the GSH level was down-regulated by decreased Zn. Consistent with this hypothesis, treatment with 7.5 μmol/L of TPEN decreased cellular Zn to ~40 fg/cell at 30 hours after treatment in PC/SEN cells (Fig. 4*A, left, solid line*). The decrease seen in PC/RES cells owing to TPEN treatment was more rapid, with the Zn concentration being reduced to ~40 fg/cell within 7 hours (Fig. 4*A, left, dashed line*). The intracellular GSH also decreased with the reduction in intracellular Zn (Fig. 4*A, right, dashed line*).

To determine the effects of TPEN on the growth of PC/RES cells, the cells were pulse-treated for 2 hours with TPEN for 5 consecutive days and the growth was examined. Although treatment with 1 μmol/L CDDP did not induce apparent morphologic changes (Fig. 4*B, bottom, left*), the combined treatment with TPEN and CDDP caused prominent changes (Fig. 4*B, bottom, right*). A colony formation assay clearly showed that the combination of CDDP and TPEN, as well as single TPEN treatment, significantly impaired the growth of PC/RES cells (Fig. 4*C*). Consistent with these changes, ICP-MS indicated that the intracellular Pt content increased 3.5-fold after the combined treatment (from 0.38 to 1.35 fg/cell with TPEN treatment). It is important to note that the same dose of TPEN did not attenuate the growth of PC/SEN cells (Fig. 4*C*). These data indicate that the GSH level seems to be critical for resistance in PC/RES cells, consistent with previous reports that CDDP-resistant cells have high levels of GSH and that a decrease in GSH results in loss of resistance (3, 19). Our data also suggest that the high GSH content was maintained by the effects of Zn in PC/RES cells. Overall, our trial treatment with combined TPEN and CDDP suggests that this combination would be effective in eliminating tumors even if they include a CDDP-resistant population of cells with high Zn content.

We showed the use of element array analysis by SXFM to examine a mechanism of CDDP resistance. Based on element profiles, we successfully overcame CDDP resistance in PC/RES cells by using a Zn chelator that down-regulated the GSH level. Although it has been reported that Cu is a necessary factor for CDDP incorporation (7), the present work revealed that Cu was not involved in PC/RES cells. It is tempting to speculate that drug resistance is generated by various elements, and we propose that an element array can contribute to better understanding of cancer biology as well as other fields of medical science.
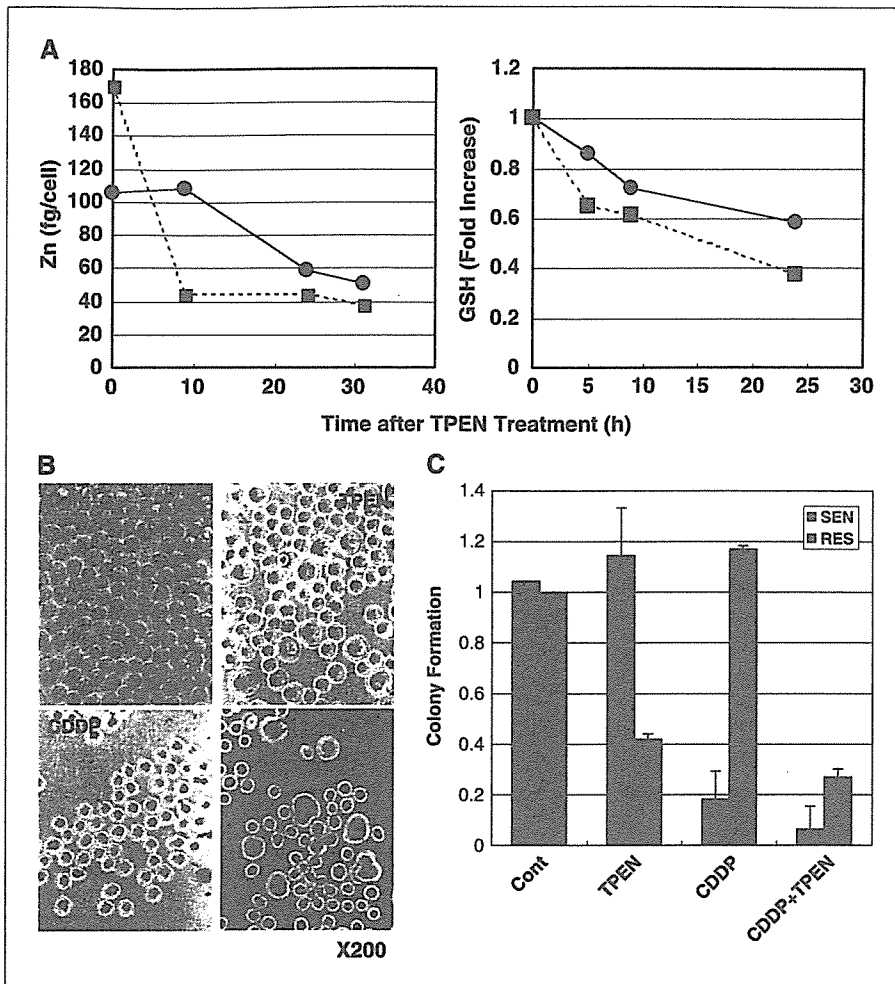
Figure 4. Cellular Zn content and Pt uptake with TPEN. *A,* TPEN-induced depletion of cellular Zn and down-regulation of GSH. TPEN (7.5 μmol/L) was added to the culture medium for the indicated time periods, and cellular Zn was measured by ICP-MS (*left*). Intracellular GSH content was also monitored (*right*). The Zn contents in PC/SEN (*solid lines*) and PC/RES cells (*dashed lines*) are shown. *B,* morphologic changes after pulse treatment with TPEN and CDDP. The morphologies of untreated PC/RES cells (*top, left*) and of cells treated with TPEN (*top, right*), CDDP (*bottom, left*), and CDDP plus TPEN (*bottom, right*) are shown. The cells were exposed to 1.0 μmol/L CDDP with or without 7.5 μmol/L TPEN for 2 hours, and then the medium was replaced with fresh medium. Pulse treatment was carried out for 5 consecutive days. Magnification, ×200. Note that large cells are observed after treatment with TPEN alone, and larger cells with irregular shape are observed following the combination treatment. The data showed that TPEN caused cellular accumulation at G_2-M phase with mitotic failure (data not shown). *C,* colony formation after pulse treatment with CDDP with or without TPEN. After pulse treatment for 5 consecutive days, as described in (*B*), the cells were plated in soft agar and the colony formation assay was done. The means and SDs of colony numbers of PC/SEN (*black columns*) and PC/RES cells (*gray columns*) are shown. The experiments were carried out in triplicate.

References

1. Boulikas T, Vougiouka M. Cisplatin and platinum drugs at the molecular level. Oncol Rep 2003;10:1663–82.
2. Kuo TH, Liu FY, Chuang CY, Wu HS, Wang JJ, Kao A. To predict response chemotherapy using [99m]technetium tetrofosmin chest images in patients with untreated small cell lung cancer and compare with p-glycoprotein, multidrug resistance related protein-l, and lung resistance-related protein expression. Nucl Med Biol 2003;30:627–32.
3. Godwin AK, Meister A, O'Dwyer PJ, Huang CS, Hamilton TC, Anderson ME. High resistance to cisplatin in human ovarian cancer cell lines is associated with marked increase of glutathione synthesis. Proc Natl Acad Sci U S A 1992;89:3070–4.
4. Ishikawa T, Wright CD, Ishizuka H. GS-X pump is functionally overexpressed in *cis*-diamminedichloroplatinum (II)-resistant human leukemia HL-60 cells and down-regulated by cell differentiation. J Biol Chem 1994;269:29085–93.
5. Mayes PA,. Nutrition. In: Murray RK, Granner DK, Mayers PA, Rodwell VW, editors. Harper's biochemistry. Chapter 54. 25th ed. New York: McGraw-Hill; 2000. p. 653–61.
6. Koropatnick J, Pearson J. Zinc treatment, metallothionein expression, and resistance to cisplatin in

mouse melanoma cells. Somat Cell Mol Genet 1990;16: 529–37.
7. Katano K, Kondo A, Safaei R, et al. Acquisition of resistance to cisplatin is accompanied by changes in the cellular pharmacology of copper. Cancer Res 2002;62:6559–65.
8. Ilinski P, Lai B, Cai Z, et al. The direct mapping of the uptake of platinum anticancer agents in individual human ovarian adenocarcinoma cells using a hard X-ray microprobe. Cancer Res 2003;63:1776–9.
9. Hall MD, Dillon CT, Zhang M, et al. The cellular distribution and oxidation state of platinum(II) and platinum(IV) antitumor complexes in cancer cells. J Biol Inorg Chem 2003;8:726–32.
10. Parat M-O, Richard M-J, Meplan C, Favir A, Béani J-C. Impairment of cultured cell proliferation and metallothionein expression by metal chelator *NNN′ N′*-tetrakis-(2-pyridylmethyl)ethylene diamine. Biol Trace Elem Res 1999;70:51–68.
11. Miao J, Hodgson KO, Ishikawa T, Larabell CA, LeGros MA, Nishino Y. Imaging whole *Escherichia coli* bacteria by using single-particle X-ray diffraction. Proc Natl Acad Sci U S A 2003;100:110–2.
12. Kirkpatrick P, Baez AV. Formation of optical images by X-rays. J Opt Soc Am 1948;38:766–74.
13. Yamauchi K, Yamamura K, Mimura H, et al. Two-

dimensional submicron focusing of hard X-rays by two elliptical mirrors fabricated by plama chemical vaporization machining and elastic emission machining. Jpn J Appl Phys 2003;42:7129–34.
14. Kawamura-Akiyama Y, Kusaba H, Kanzawa F, Tamura T, Saijo N, Nishio K. Non-cross resistance of ZD0473 in acquired cisplatin-resistant lung cancer cell lines. Lung Cancer 2002;38:43–50.
15. Richarz AN, Wolf C, Bratter P. Determination of protein-bound trace elements in human cell cytosols of different organs and different pathological states. Analyst 2003;128:640–5.
16. Glantz SA. How to test for trends. In: Glantz SA, editors. Primer of biostatistics. Chapter 8. 2nd ed. New York: McGraw-Hill; 1987. p. 191–244.
17. Jourdan E, Jeanne RM, Régine S, Pascale G. Zinc-metallothionein genoprotective effect is independent of the glutathione depletion in HaCaT keratinocytes after solar light irradiation. J Cell Biochem 2004;92:631–40.
18. Parat M-O, Richard M-J, Béani J-C, Favier A. Involvement of zinc in intracellular oxidant/antioxidant balance. Biol Trace Elem Res 1997;60:187–204.
19. Hamaguchi K, Godwin AK, Yakushiji M, O'Dwyer PJ, Ozols RH, Hamilton TC. Cross-resistance to diverse drugs is associated with primary cisplatin resistance in ovarian cancer cell lines. Cancer Res 1993;53:5225–32.

— 43 —

In this brief review of achievements in "Life Science" obtained in SPring-8, I chose four research works among others because of their unique applications, i.e., (i) X-ray fluorescence microscopy for cellular mineral analysis, (ii) phase contrast X-ray imaging of fetal lungs, (iii) synchrotron radiation CT for the analysis of small-airway deformation and (iv) X-ray diffraction recording from a single sarcomere.

Ishizaka et al. utilized scanning X-ray fluorescence microscopy (SXFM) to detect minerals at the cellular level. They visualized platinum (Pt) with other elements in mammalian cells after treatment with an anticancer agent, cis-diamminedichloro platinum (II) (CDDP). They composed PC-9 cells (originally derived from a lung carcinoma) sensitive (PC/SEN) and resistive (PC/RES) to CDDP. Twelve hours after CDDP treatment, the level of Pt increased in PC/SEN cells, but it changed little in PC/RES cells, indicating that an enhanced accumulation of CDDP in the cells is responsible for the hypersensitivity of PC/SEN cells. They also found that the Zn level is high in untreated PC/RES cells with elevated intracellular glutathione level. They concluded that this method is useful for the better understanding of cancer biology.

Hooper et al. applied phase contrast X-ray imaging (PCXI) to evaluate the pattern of lung aeration of rabbit pups at birth. Lung images were analyzed before a breath or at fixed time intervals after birth. They found that PCXI was able to resolve terminal respiratory units, and air-filled structures gave them "speckle" appearances. The pattern of lung aeration was very dependent upon body position and was heavily influenced by respiratory activity. The increase in air volume can be calculated from the projected thickness of the lung image.

Sera et al. determined the localized morphometric deformation of small airways and alveoli using a synchrotron radiation CT system. Euthanized mice were mounted on the rotation stage of the CT system under quasi-static inflation to mimic respiration. They visualized the same airways of the same lung at functional residual capacity (FRC) and total lung capacity (TLC). The length (L) and diameter (D) of airway segments were measured, and the increases in L and D, i.e., ΔL and ΔD were normalized by FRC. Results showed that ΔD was larger than ΔL and both values were greater for a smaller-airway group. Thus, airways may deform differently depending on their size and tissue anisotropism.

Iwamoto et al. developed a technique of quick-freezing specimens of myofibrils isolated from an insect flight muscle. X-ray diffraction using microbeams was carried out to analyze the local structure. The strongest equatorial reflections (1.0 and 2.0) were observed. However, the 1.1 reflection was missing in the diffraction pattern of a myofibril, unlike in that of muscle. Because the beam diameter was ~2 μm, i.e., smaller than that of a single sarcomere, the diffraction should come from a single sarcomere within a single myofibril.

In summary, X-ray fluorescence microscopy, phase contact X-ray imaging, synchrotron radiation CT and X-ray diffraction method offer powerful tools for micro- or nano-order biological analysis.

Fumihiko Kajiya
Kawasaki Medical School
Okayama University

Minerals are essential for many cellular functions, and iron, magnesium, cobalt, and manganese are well characterized with respect to their roles in enzymatic catalysis. Zinc (Zn) is also a requirement for cell growth and survival, and essential for the activity of zinc-metalloenzymes that participate in cell metabolism. To clarify the biological roles of these ions it is important to characterize elements in individual cells. Highly coherent X-rays from third-generation synchrotron sources are opening up various new possibilities of nano-imaging for application in cellular biology. Although recently developed scanning X-ray fluorescence microscopy (SXFM) enable the detection of elements at cellular the level [1,2], higher resolution is still expected for imaging intracellular elements. Yamauchi et al. have developed a Kirkpatric-Baez (K-B)-type X-ray focusing system [3] in which, using the 1 km beamline of SPring-8, elliptically figured mirrors focus coherent X-rays to various spot sizes selectively on the demand of spatial resolution, sensitivity and time. As the first application of this method, we visualized platinum (Pt) alongside other cellular elements in mammalian cells after treatment with cis-diamminedichloro platinum (II) (CDDP) [4].

CDDP is an effective anti-cancer agent, but tumor cells can become resistant after CDDP-based therapy [5]. We measured intracellular elements by SXFM before and after treatment with CDDP and compared the element profiles of PC-9 cells (PC/SEN) which are originally derived from a lung carcinoma and PC-9 sublines resistant to CDDP (PC/RES). SXFM was set up at the undulator beamline **BL29XU** by combining the K-B-type X-ray focusing system [3], an xy-scanning stage for sample mounting, and an energy-dispersive X-ray detector. Monochromatic X-rays at 15 keV for Pt L-line excitation were focused into a 1.5 μm (H) $\times$ 0.75μm (W) spot with a measured flux of ~1 $\times 10^{11}$ photons/s. The focused X-rays simultaneously yielded the fluorescence of various chemical species in a small volume of sample cells (Fig. 1(a)). After counts were collected for 4.0-8.5 sec at each pixel of scanning, the counts were normalized with incident beam intensity. Elemental concentration per cell was also calculated from integrated elemental intensity over the entire mapping image.

Twelve hours after treatment with CDDP, the level of Pt increased in PC/SEN cells, whereas a slight increase in Pt level was observed in PC/RES cells (Fig. 1(b)). The signal intensity of Pt in PC/RES cells was 2.6-fold less than that in PC/SEN cells [4]. The
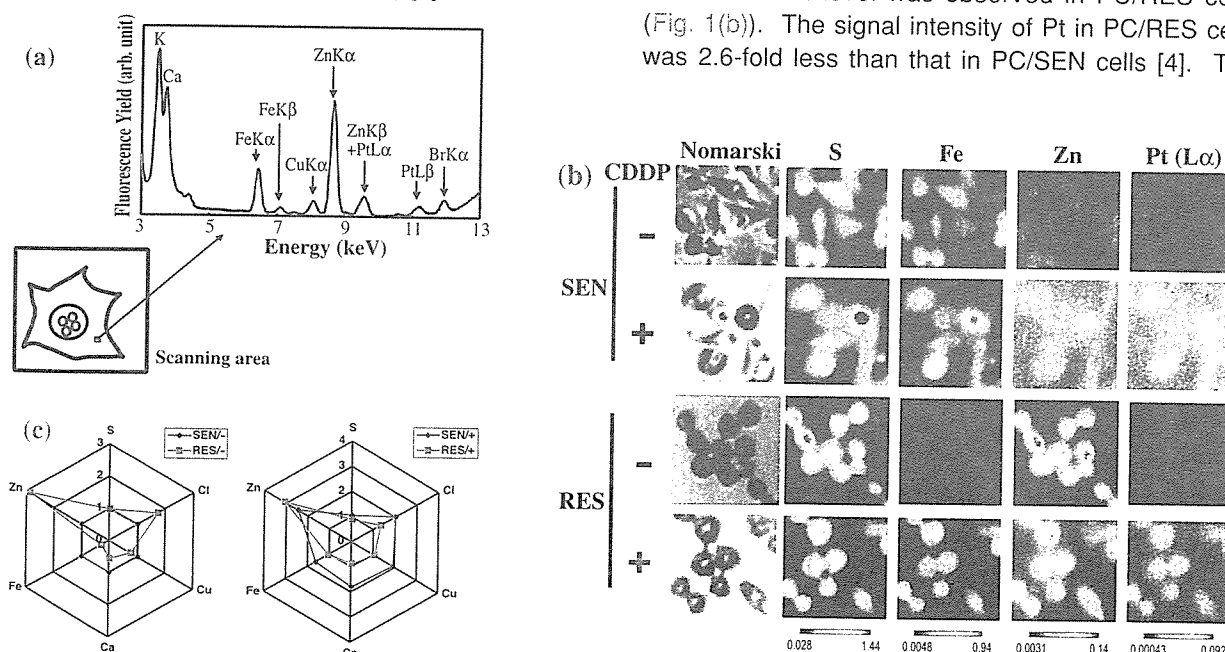
Fig. 1. Element array analysis. (a) Scheme of imaging cellular elements by SXFM. (b) SXFM analysis of original PC-9 cells (SEN) and subline cells (RES) resistant to CDDP after CDDP treatment (+) and under CDDP free condition (-). Brighter colors indicate a higher signal intensity of each element. (c) Element array based on SXFM analysis.

decreased accumulation of CDDP is therefore likely responsible for resistance in PC/RES cells, which is consistent with the finding that the excretion of CDDP may be one of the major factors contributing to CDDP resistance [5]. On the base of the mean signal intensity obtained by SXFM, element array analysis was carried out (Fig. 1(c)). We noted that the Zn content of untreated PC/RES cells was approximately 3-fold that of PC/SEN cells (Fig. 1(c), left panel). When CDDP was used for treatment, the high content of Zn was observed most markedly in both cell lines (Fig. 1(c), right panel).

We next focused on a zinc-related excretion system to clarify the role of Zn in a mechanism underlying resistance to CDDP. We found that the level of intracellular glutathione (GSH) was constitutively high in PC/RES cells (Fig. 2(a)), showing a significant correlation with the levels of Zn detected by both ICP-MS and SXFM (Pearson product-moment correlation coefficient r. 0.794, $P < 0.05$ and r. 0.533, $P < 0.05$, respectively) (Fig. 2(b)). Consistent with these observations, a Zn (II) chelator, N,N,N',N'-tetrakis-(2-

pyridylmethl)-ethylenediamine (TPEN), decreased both cellular Zn and GSH level in PC/RES cells [4], making PC/RES cells sensitive to CDDP (Fig. 3).

In the current study, we demonstrated the use of element array analysis by SXFM for examining a mechanism of CDDP resistance. We propose that element array analysis is a powerful tool contributing to a better understanding of cancer biology as well as other fields of medical science. We expect that researchers in various life science fields would join in this promising project.
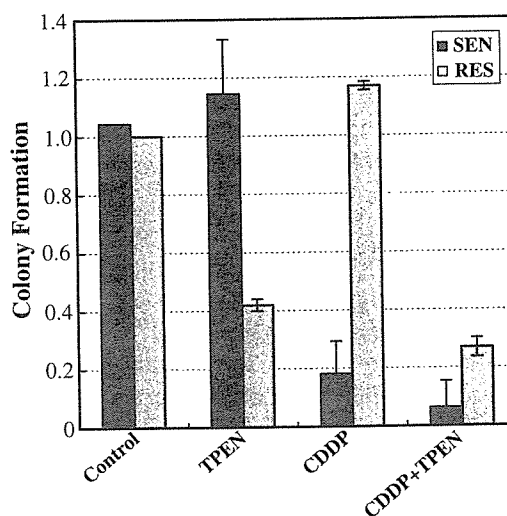
Fig. 3. Colony formation after treatment with CDDP and/or TPEN (Zn (II) chelator), which shows the effectiveness of the treatments to the cell viability. Control shows the result for treatment-free cells for comparison. Cells entitled by TPEN or CDDP + TPEN were pulse-treated for 2 h with TPEN for 5 consecutive days. The ability for colony formation, the aggregation of more than 50 cells arising from a single surviving cell, was examined.
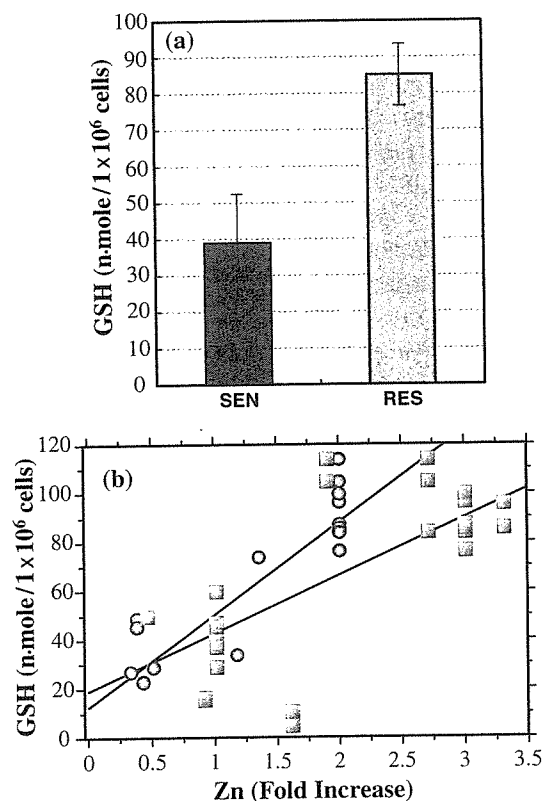

Fig. 2. (a) Basal level of intracellular GSH. (b) Correlation between Zn and intracellular GSH levels. A scatter diagram for Pearson product-moment correlation coefficient is shown. Zn level, measured by SXFM (red squares, $n = 27$) and ICP-MS (green circles, $n = 29$), was plotted against intracellular GSH level.

Mari Shimura[a], Akira Saito[b] and Yukihito Ishizaka[a],*

[a] Department of Intractable Diseases, International Medical Center of Japan
[b] Department of Material and Life Science, Osaka University

*E-mail: zakay@ri.imcj.go.jp

References

[1] P. Ilinski et al.: Cancer Res. 63 (2003) 1776.
[2] M.D. Hall et al.: J. Biol. Inorg. Chem. 8 (2003) 726.
[3] K. Yamauchi et al.: J. Appl. Phys. 42 (2003) 7129.
[4] M. Shimura, A. Saito, S. Mastuyama, T. Sakuma, Y. Terui, K. Ueno, H. Yumoto, K. Yamauchi, K. Yanamura, H. Mimura, Y. Sano, M. Yabashi, K. Tsmasaku, K. Nishio, Y. Nishino, K. Endo, K. Hatake, Y. Mori, Y. Ishizaka and T. Ishikawa: Cancer Res. 65 (2005) 4998.
[5] K. Zhang et al.: Mol. Pharmacology. 59 (2001) 837.

Cell-cycle-dependent dynamics of nuclear pores: pore-free islands and lamins

Kazuhiro Maeshima[1],*, Kazuhide Yahata[2], Yoko Sasaki[1], Reiko Nakatomi[3], Taro Tachibana[4], Tsutomu Hashikawa[3], Fumio Imamoto[2] and Naoko Imamoto[1],*

[1]Cellular Dynamics Laboratory, Discovery Research Institute, RIKEN, 2-1 Hirosawa, Wako-shi, Saitama, 351-0198 Japan
[2]Department of Molecular Biology, BIKEN, Osaka University, Osaka, Japan
[3]Laboratory for Neural Architecture, Brain Research Institute, RIKEN, Wako-shi, Japan
[4]Department of Bioengineering, Graduate School of Engineering, Osaka City University, Osaka, Japan
*Authors for correspondence (e-mail: maeshima@riken.jp; nimamoto@riken.jp)

Summary

Nuclear pores are sophisticated gateways on the nuclear envelope that control macromolecular transport between the cytoplasm and nucleoplasm. So far the structural and functional aspects of nuclear pores have been extensively studied, but their distribution and density, which might reflect nuclear organization and function, remain unknown. Here, we report the cell-cycle-dependent dynamics of nuclear pores. Large distinct subdomains lacking nuclear pores are present on the nuclear surface of HeLaS3 cells in early cell-cycle stages. Such 'pore-free islands' gradually become dispersed in G1-S phase. Surprisingly, the islands are enriched with inner nuclear membrane proteins lamin A/C and emerin, but exclude lamin B. Lamin-A/C-enriched pore-free islands were also observed in human normal diploid fibroblasts and several cell lines, showing the generality of this phenomenon. Knockdown and ectopic expression analyses demonstrated that lamin A/C, but not emerin, plays an essential structural and regulatory role in the nuclear pore distribution and the formation of pore-free islands. These data thus provide strong evidence that the dynamics of nuclear pores are regulated by the reorganization of inner nuclear structures.

Supplementary material available online at
http://jcs.biologists.org/cgi/content/full/119/21/4442/DC1

Key words: Emerin, Cell cycle, Lamin A/C and lamin B, Nuclear pores, Nuclear structure

Introduction

The eukaryotic nucleus is a complex and sophisticated organelle that contains genomic chromatin, and supports many essential cellular activities, including DNA replication, RNA transcription and processing, and ribosome assembly. Such nuclear functions are largely dependent upon the structural organization of the nucleus and the formation of a membranous structure, the nuclear envelope (NE), which separates the nucleoplasm from the cytoplasm (Gerace and Burke, 1988). The nuclear envelope consists of an inner and outer nuclear membrane, nuclear pores, and the underlying nuclear lamina, a filamentous meshwork (Goldman et al., 2002).

The core meshwork structure of the lamina is formed by type-V intermediate filament proteins called lamins, which are composed of B-type (lamin B1-3) and A-type lamins (lamin A and its short splicing variant, lamin C) (Aebi et al., 1986; Stuurman et al., 1998). While B-type lamins are constitutively expressed in cells throughout development, A-type lamins (lamin A/C) are only expressed in later stages of development and in differentiated cells (Hutchison et al., 2001). The importance of lamins has been demonstrated by several recent findings: genetic approaches in Drosophila melanogaster (Lenz-Bohme et al., 1997), Caenorhabditis elegans (Liu et al., 2000), and cultured mammalian cells (Harborth et al., 2001), all of which suggest that B-type lamins are essential for

viability. The targeted disruption of lamin A/C in mice causes muscular dystrophy, loss of adipose tissue and early death (Sullivan et al., 1999). In addition, mutations in the lamin A/C gene, as well as in several genes that encode inner nuclear membrane proteins that bind to the lamina, have been shown to cause a variety of human genetic disorders: the so-called 'laminopathies', including Emery-Dreifuss muscular dystrophy and Hutchinson-Gilford progeria syndrome (HGPS) (Burke and Stewart, 2002; Hutchison and Worman, 2004; Mounkes et al., 2003; Wilson, 2000).

In addition to the nuclear membrane and the nuclear lamina, nuclear pores are genuine constituents of the nuclear envelope. In eukaryotic cells, all macromolecules that are transported between the nucleus and the cytoplasm cross the nuclear membrane through nuclear pore complexes (NPCs) (Imamoto, 2000). NPCs are elaborate gateways that allow the translocation of a variety of macromolecules in an efficient but selective fashion (Cronshaw et al., 2002; Gorlich and Kutay, 1999; Macara, 2001; Rout et al., 2000). In vertebrate cells, NPCs are cylindrical structures consisting of multiple copies of about 30 different proteins called nucleoporins, with a diameter of 120 nm, a thickness of 70 nm, and a mass of approximately 100 MDa (Davis, 1995; Fahrenkrog et al., 2004; Hetzer et al., 2005; Rout and Wente, 1994; Suntharalingam and Wente, 2003; Vasu and Forbes, 2001). However, how, when and where these nucleoporins converge

to form a nuclear pore remains largely unknown. Once formed on the nuclear membrane, NPCs have static and immobile nature, suggesting that they are physically linked to intranuclear structures such as the nuclear lamina, inner nuclear membrane proteins, and chromatins (Daigle et al., 2001; Rabut et al., 2004).

Since a number of previous studies have just focused on gating properties and structural analyses of nuclear pores to understand the transport mechanism, exploring the behavior of nuclear pores would also be of interest. Several earlier reports demonstrated that the number of nuclear pores increases during the cell cycle (Maul et al., 1971) or in response to hormone stimulation (Maul et al., 1980; Oberleithner et al., 1994). Highly proliferative cells such as embryos or tumors have a high density of nuclear pores, whereas terminal differentiated cells such as erythrocytes have much fewer (Maul et al., 1980). These observations imply that the density of nuclear pores might be correlated with the cellular metabolic activity. More recently, it was shown that components of nuclear pores are implicated in the spatial gene regulation, suggesting the structural roles for nuclear pores in the nuclear organization and function (Casolari et al., 2004; Ishii et al., 2002; Schmid et al., 2006). These observations suggest a highly dynamic aspect of nuclear pores, and raise the question of whether certain cellular events can determine the behavior of nuclear pores.

To address this question, we investigated the dynamics of nuclear pore distribution and density in human cells. We initially found novel and unique subdomains on the nuclear envelope of HeLa S3 cells, which resembles large "islands" that are devoid of nuclear pores. An examination throughout the cell cycle revealed that such pore-free islands are present in the telophase and in most G1 phase nuclei. This pore-free island gradually disperses, and pore density concomitantly increases, as the cell cycle progresses to the S phase. Surprisingly, some inner nuclear membrane proteins including emerin and lamin A/C, but not lamin B, are highly enriched in the pore-free islands. Uneven distributions of nuclear pores and dynamic changes were also observed in human osteosarcoma U-2 OS and in human IMR90 normal diploid fibroblasts. siRNA-mediated knockdown of lamin A/C resulted in the disappearance of pore-free islands, whereas the upregulation of lamin A/C stabilized and/or facilitated formation of pore-free islands. Our present results show that lamin A/C plays an essential structural and regulatory role in pore distribution, and also determine the nuclear subdomains, where nucleocytoplasmic transport could be suppressed as a function of cell growth and differentiation.

Results

Dynamic change(s) of nuclear pore distributions during the cell cycle

With the recent development of fluorescence microscopy imaging, it has become possible to visualize a single nuclear pore on the nuclear surface, by immunostaining with antibodies that recognize the nuclear pore components (inset in Fig. 1A1) (Kubitscheck et al., 1996). To investigate nuclear pore distributions and density in a HeLa S3 cell line, nuclear pores in asynchronous cells were immunostained. Bright punctate rim
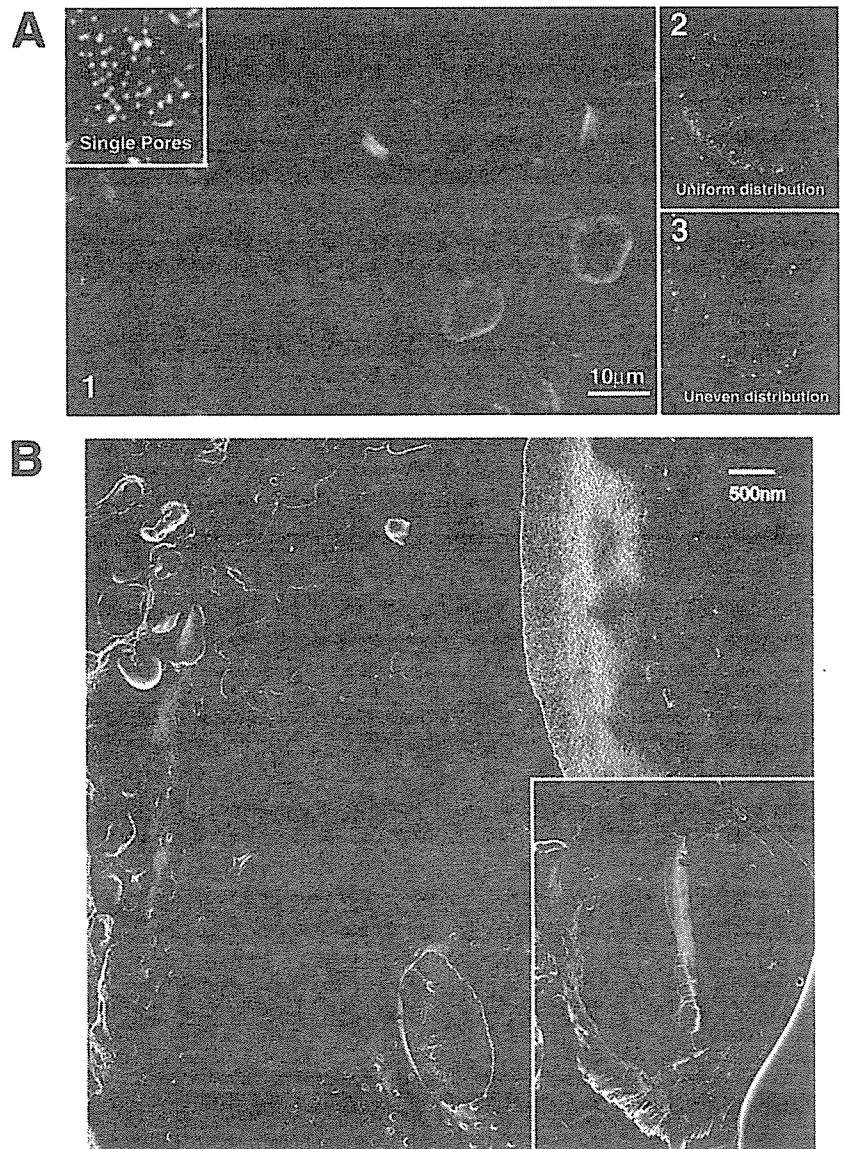

Fig. 1. Heterogeneous distribution of nuclear pores. (A1) Low-magnification image of asynchronous HeLa S3 nuclear surfaces stained for nuclear pores with anti-p62 antibody. Note that the nuclear pore distributions are surprisingly heterogeneous from nucleus to nucleus. Inset, visualization of single nuclear pores at high magnification. (A2) Nucleus with an almost uniform pore distribution. (A3) Nucleus with a large 'island' that is devoid of nuclear pores. (B) Direct observation of nuclear pores and pore-free islands by scanning electron microscopy. A nuclear surface of freeze-fractured early G1 HeLaS3 cells (inset) and its enlarged image. Many nuclear pores are clearly visible. A large pore-free island is spread on the smooth inner nuclear envelope, demonstrating the integrity of the nuclear envelope.

staining was observed on the nuclear equator (supplementary material Fig. S1A). However, an examination of the nuclear surface (adjacent to the growth surface) revealed that the nuclear pores were strikingly unevenly distributed (Fig. 1A1): some nuclei showed an almost uniform pore distribution (Fig. 1A2), whereas other nuclei contain large 'islands' that are devoid of nuclear pores (Fig. 1A3). Such large pore-free islands comprise as much as 40% of the nuclear surface. These pore-free islands were also observed by a stable expression of nucleoporin p62 conjugated to Venus (a bright YFP derivative) (Nagai et al., 2002) in the HeLaS3 cells, ruling out the possibility that this is due to a staining artifact (supplementary material Fig. S1C). In addition to the visualization of nuclear pores by immunostaining and ectopic expression of fluorescent nucleoporin, freeze-fractured samples of HeLaS3 cells were prepared and observed by a cryo-scanning electron microscopy to directly visualize the nuclear pores and pore-free islands. An enlarged image (Fig. 1B) clearly demonstrates a large pore-free island spreading onto the smooth and continuous nuclear envelope.

If the nuclear pore distribution is assumed to be random and obey a Poisson distribution, the probability of forming a 30 μm^2 pore-free island, as is typically found, will be about 10^{-79} (see Materials and Methods). This implies that the pore-free island is not formed by chance. It is thus conceivable that a specific structure contributes to make the regions pore-free. What could cause such uneven pore distributions, forming pore-free islands? What is the structural organization of the pore-free islands? These questions were addressed in the following studies.

We first wondered whether differences in the pore distribution were correlated with cell cycle progression. To test this possibility, the

distribution of nuclear pores throughout the HeLa S3 cell cycle was investigated using three cell cycle markers, Ki67, PCNA and CENP-F, which are useful in identifying the G1, S and G2 stages, respectively. The nuclei with small Ki-67 discrete foci characteristics of early G1 cells (Kill, 1996), have large pore-free islands on the nuclear surface (supplementary material Fig. S4A). A quantitative analysis showed that 90% of the early G1 nuclei contained such pore-free islands on the top and/or bottom surface (Table 1). In the early S-phase, PCNA foci are distributed throughout the nucleoplasm although they are absent in G1 and G2 nuclei. A nucleus with such PCNA foci has a smaller pore-free island whereas the paired nuclei without PCNA signal, presumably in the G1 phase, possess large pore-free islands on the surfaces (Fig. 2A). Nuclei in mid-to-late S phase, represented by PCNA foci that are larger in size and fewer in number (Dimitrova et al., 1999), show a much more uniform pore distribution and contain a number of small pore-free islands (Fig. 2A, top panels). The percentage of nuclei with large pore-free islands dropped to 26% at this stage (Table 1). G2-phase nuclei, which are highly positive for
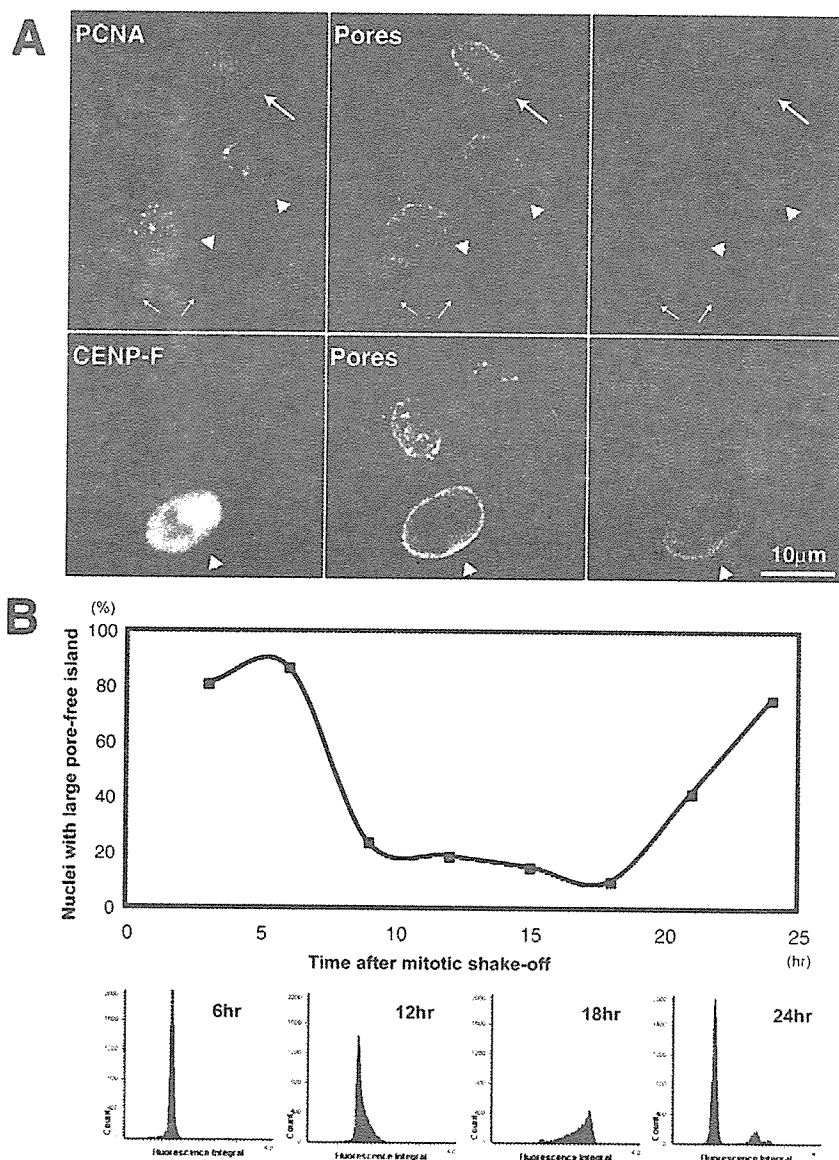

Fig. 2. (A) Cell-cycle dependency of nuclear pore distribution in HeLaS3 cells. Nuclei were co-stained for nuclear pores (center column) and PCNA (top panels) or G2 marker CENP-F (bottom panels). The paired nuclei without PCNA signal, probably in G1 phase, possess large pore-lacking islands (top panels, small arrows), whereas the nucleus with early-S PCNA foci (large arrows) has a smaller pore-free island. The two nuclei with large and few PCNA foci (top panels, arrowheads), characteristics of mid-late S-phase nuclei, have a much more uniform pore distribution. The nucleus with CENP-F signal has uniform pore distributions (bottom panels, arrowheads). Nuclei without CENP-F have large pore-free islands on the nuclear surface. Asynchronous cells were used in these experiments. (B) Dispersal of pore-free island with cell-cycle progression. Synchronized mitotic HeLaS3 cells were collected and released at 0 hour. After 3, 6, 9, 12, 15, 18, 21, 24 hours, the number of nuclei in which more than 30% of the surface is comprised of pore-free islands, was counted and shown as a percentage. Cell-cycle profiles of the released cells at the indicated time-points were obtained with an Olympus LCS2, demonstrating cell-cycle progress in a time-dependent manner (histograms).

Table 1. Quantitative analysis of the pore-free islands in various cell-cycle stages

Cell-cycle stage	Marker	Nuclei with pore-free islands*
Telophase and cytokinesis		100 / 100
Early G1	Ki-67	89 / 100
Early S	PCNA	50 / 100
Mid to late S	PCNA	26 / 100
G2	CENP-F	9 / 100
Late G2 to prophase[‡]	CENP-F	6 / 100

*The number of nuclei in which more than 30% of the surface is comprised of pore-free islands (n=100 cells). ‡Nuclei with enrichments of CENP-F at the centromere regions.

CENP-F signals (Liao et al., 1995), show rather uniform pore distributions (Fig. 2A, bottom panels). At this stage, fewer than 10% of the nuclei contain pore-free islands on the surface (Table 1). The series of cell-cycle analysis evidently shows that pore-free islands disperse with cell-cycle progression. To confirm this finding, we collected synchronized mitotic cells, released them, and counted the number of nuclei with large pore-free island at various time points (Fig. 2B). In good agreement with the analysis using cell-cycle markers, the number of nuclei with large pore-free islands decreases with cell cycle progression.

A quantitative analysis revealed that the average pore density on the G1 nuclear surface, including the pore-free island, is about 5 NPCs/μm^2. The pore density in G2 cells increases to 8.56 ± 0.34 NPCs/μm^2. The disappearance of the pore-free island is likely to be correlated with the increase in pore density (see below and Discussion). The nuclear pore distributions thus drastically change, from uneven to even, with increase in pore density as the cell cycle progresses in HeLa S3 cells.

Structural organization of the pore-free islands

As described above, HeLa S3 nuclei contain large pore-free islands in the early stages of the cell cycle. The next obvious question is what is the structural organization of the pore-free islands. To answer this question, the internal nuclear structure of the pore-free islands was examined by immunostaining several inner nuclear membrane proteins. Fig. 3A (fourth row) shows that lap2β is distributed almost uniformly on the nuclear surface in G1 phase, showing the integrity of the nuclear envelope. We found, however, that emerin and lamin A/C, which are linked to a variety of human genetic disorders (laminopathies) including Emery-Dreifuss muscular dystrophy, are highly enriched in the pore-free islands (Fig. 3A, first and third rows and supplementary material Fig. S1B). Co-immunostaining of nuclear pores and emerin or lamin A/C shows an apparently complementary pattern. Ectopic co-expression of CFP-emerin and p62-Venus also show a complementary pattern, confirming the immunostaining result (supplementary material Fig. S1C). At telophase, emerin accumulates in the pore-free islands on both sides of the newly reformed nuclei (Fig. 3A, second row). This observation is reminiscent of the 'core' region proposed by Haraguchi et al. (Haraguchi et al., 2000; Haraguchi et al., 2001), suggesting that the pore-free islands originate from the telophase
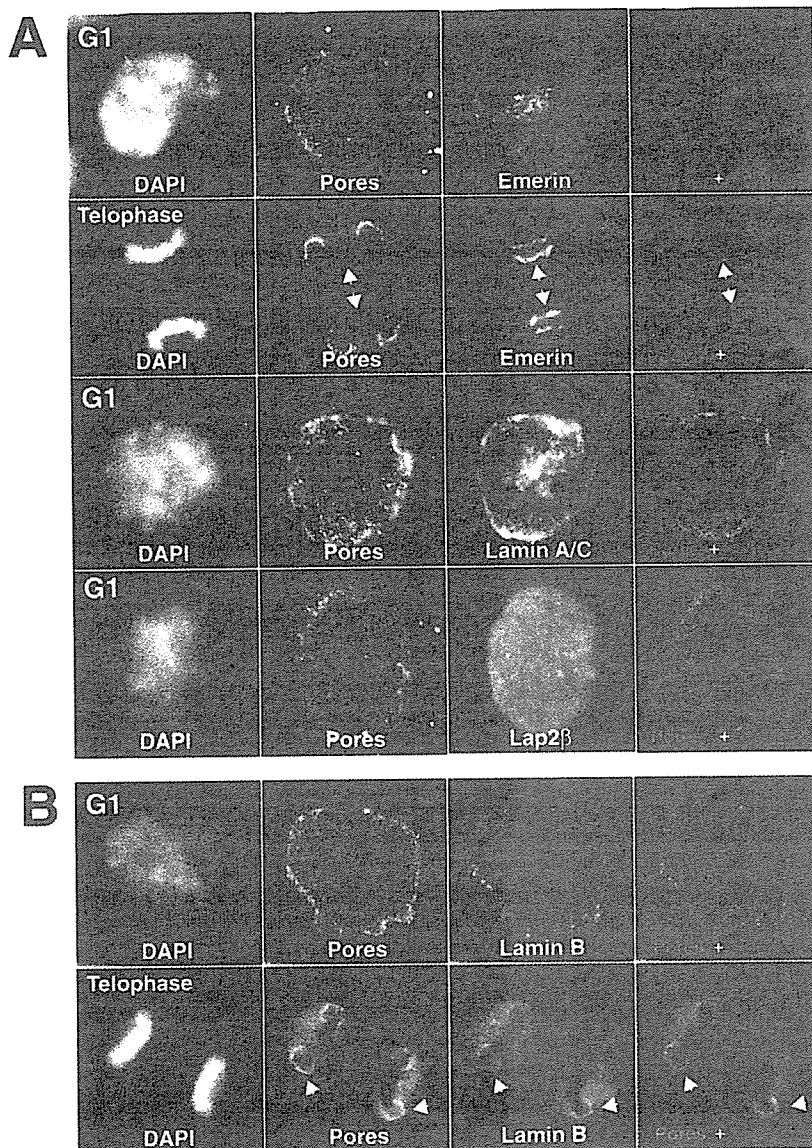

Fig. 3. Structural organization of pore-free islands. (A) Accumulation of inner nuclear membrane proteins emerin and lamin A/C in the pore-free islands. Nuclei co-stained for nuclear pores and inner nuclear membrane proteins: emerin (top two rows), lamin A/C (third row) and lap2β (fourth row). Emerin and lamin A/C are enriched in the pore-free islands of G1 (first and third rows) and telophase (second row) nuclei. Note that lap2β is almost uniformly distributed on the surface of the G1 nucleus (fourth row). (B) Lamin B is excluded from the pore-free island. Surface image of the G1 nuclei (top panels) and middle section of the telophase nuclei (bottom panels), co-stained with DAPI, nuclear pores and lamin B. Merged images of nuclear pores and lamin B are shown on the right. Note that nuclear pores colocalized well with lamin B both in telophase and G1 nuclei (arrowheads).
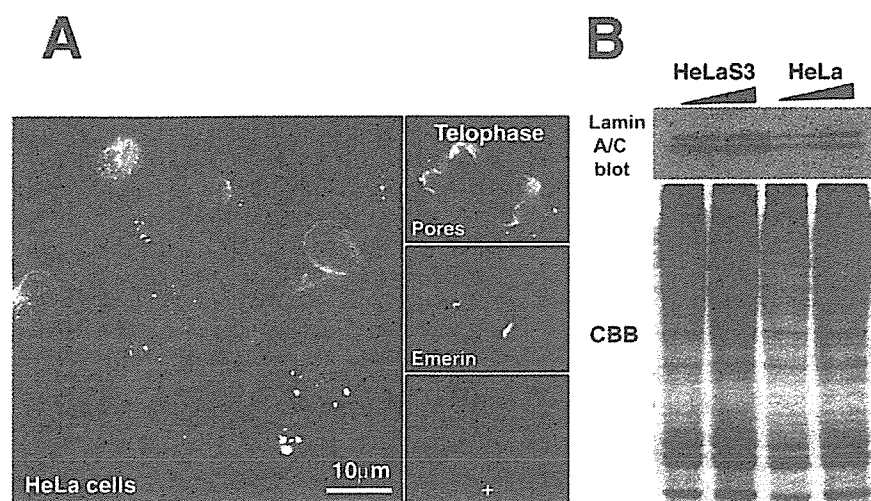
Fig. 4. Expression levels of lamin A/C affect the nuclear pore dynamics. (A) Low-magnification image of nuclear pore staining of asynchronous HeLa nuclear surfaces. The nuclear pores in most of the cells show more uniform distributions, compared with those of HeLa S3 cells shown in Fig. 1A and Fig. 3A. HeLa telophase nuclei co-stained for emerin and nuclear pores, demonstrated notable pore-free islands enriched with emerin ('core' regions) (right). (B) A-type lamins are upregulated by 4.25 times in HeLaS3 cells that contain distinct pore-free islands. Expression levels of lamin A/C in HeLaS3 cells (left two lanes) and the HeLa cells (right two lanes) shown in A were examined by western blotting. Cell lysate, equivalent to 0.5×10^4 (left) or 1×10^4 (right) cells, was loaded per lane for each cell type and verified by Coomassie Brilliant Blue (CBB) staining (bottom panel).

'core' regions. Notably, G1-phase nuclei possess emerin- and lamin A/C-accumulated islands on the top and bottom surfaces of the nuclei (Fig. 3A, first and third rows). This observation also suggests that telophase cells fall to one side and become flat during the progression from telophase to G1 phase. In contrast to A-type lamins, the staining signal for lamin B, which is an ubiquitously expressed lamin, was almost absent from the pore-free islands in both G1 and telophase nuclei, showing a very similar localization to that of the nuclear pores (Fig. 3B). Consistent with this result, lamin B receptor (LBR) is also localized in the pore region, which is complementary to the emerin staining (supplementary material Fig. S2A). We thus defined the pore-free islands as emerin- and lamin A/C-enriched areas.

Role of lamin A/C in the organization of the pore-free islands

In the course of our investigation, we noticed that some other HeLa cell lines show more-uniform pore distributions (Fig. 4A, left panel). In such HeLa cell lines, newly assembled nuclei in the telophase all contained large pore-free islands that were enriched with emerin (Fig. 4A, right panels). However, the timing of dispersal of the pore-free islands differed among HeLa cell lines and appeared to be correlated with their proliferation activity: cells that retain pore-free islands longer, have a lower proliferation activity, and vice versa (supplementary material Fig. S5C and also discussed below). In the most rapidly growing HeLa cells, the large pore-free islands appear to disperse rather quickly, consistent with the findings reported by Haraguchi et al. (Haraguchi et al., 2000; Haraguchi et al., 2001). Thus, some variations in the dynamics of nuclear pore distributions exist among HeLa cell lines. If so, what could cause such variation?

We were first concerned that the HeLa S3 cells underwent mutation(s) in the inner nuclear membrane proteins organizing the nuclear structure. To rule out this possibility, cDNAs of several inner nuclear membrane proteins (BAF, emerin, lamin A, lamin C) were isolated from the HeLa S3 cells and sequenced. No mutations were found in the sequences in any of these cDNAs (data not shown). The expression levels of the inner nuclear membrane proteins were next examined by western blotting. In the HeLa S3 cell line, the expression of lamin A/C

is upregulated 4.25 times, compared with the HeLa cell line in which the pore-free islands disperse rather quickly (Fig. 4B).

To examine an involvement of lamin A/C in pore distribution more directly, we carried out the knockdown of emerin or lamin A/C using an siRNA system (Elbashir et al., 2001; Harborth et al., 2001). The reduction of emerin and lamin A/C were clearly observed within 72 hours of RNA transfection (Fig. 5A,B). In the emerin-reduced cells, the large pore-free islands were apparently unaffected (Fig. 5B). By contrast, in lamin-A/C-depleted cells (Fig. 5A), the pore-free islands were drastically dispersed. The enlarged images (Fig. 5A, bottom panels) show some narrow regions containing residual lamin A/C. The narrow regions are almost completely devoid of nuclear pores, showing they are organized in mutually exclusive patterns on the nuclear envelope. The cell-cycle profile of the lamin-A/C-knockdown cells was indistinguishable from that of control cells (Fig. 5A), excluding the possibility that S phase or G2 phase retardation in the knockdown cells could cause dispersion of the pore-free islands. These results demonstrate that lamin A/C has an essential role in the formation of pore-free islands and that emerin is just a 'passenger' on the islands without a direct activity in pore dynamics.

In a complementary experiment, we examined whether the ectopic expression of lamin A/C can induce pore-free islands in the HeLa cell line which possess uniformly distributed pores. For this, Venus-tagged lamin A driven by the EF1α promoter was transiently expressed in the HeLa cells and the nuclear pore distributions were then examined (Fig. 6). The expressed Venus-lamin A was located at the rim of the nuclei within 48 hours after transfection, indicating the successful incorporation of Venus-lamin-A into the nuclear envelope (not shown). On the surface of these nuclei, Venus-lamin-A were enriched in discrete regions, and nuclear pores were excluded from such lamin-A-enriched regions, leading to the formation of the pore-free islands (Fig. 6), whereas the localization of lamin B was rather similar to that of Venus-lamin-A (not shown). Moreover, the lamin-A enrichment induced the clustering of nuclear pores. These results demonstrate that an ectopic expression of lamin A effectively facilitates the formation of pore-free islands on the nuclear envelope. Considering the above findings, we conclude that lamin A/C
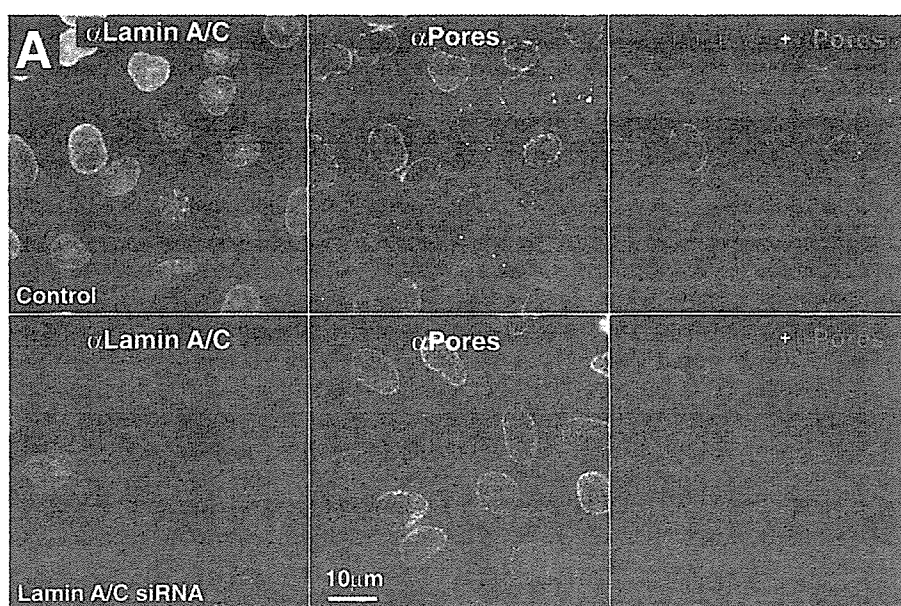
Fig. 5. Depletion of lamin A/C specifically disperses the pore-free island.
(A) Knockdown of lamin A/C by siRNA results in dispersal of the pore-free islands in HeLaS3 cells. Top panels, control cells (no RNA transfection) co-stained with nuclear pores (center) and lamin A/C (left). Bottom panels, siRNA-transfected cells co-stained with the same set of antibodies. Note that the pore-free islands in lamin A/C-depleted cells are significantly reduced. Lower images are enlarged images of a lamin A/C-reduced nucleus, showing a narrow region where residual lamin A/C has accumulated. This narrow region is almost completely devoid of nuclear pores. The histograms show DNA content of the control and knockdown cells, suggesting no significant difference in cell-cycle profile. (B) Knockdown of emerin in HeLaS3 cells. In contrast to the lamin A/C-depleted cells (A), the emerin-reduced cells still contain the large pore-free islands. This indicates that emerin itself is not directly involved in determining nuclear pore distribution.
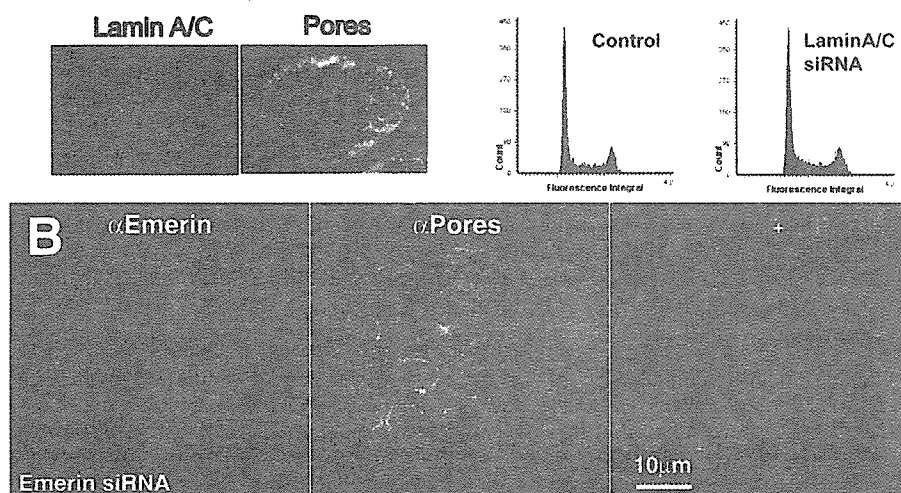
could indeed control the nuclear pore distribution in HeLa cells.

Generality of nuclear pore dynamics and underlying structural organizations

It is of particular interest to know whether the uneven pore distributions and their cell-cycle-dependent dynamics are general phenomena. Examination of nuclear pore distributions in human osteosarcoma U-2 OS cells revealed conserved pore-free islands enriched with lamin A/C, and their dispersion induced by cell-cycle progression (supplementary material Fig. S2B). Similar observations were also obtained from a colorectal cancer cell-line HCT119 cells (not shown). In addition to these transformed cell lines, we examined IMR90, human normal diploid fibroblasts. In the early stage (telophase to G1), the nuclear pores show strikingly patched distributions (Fig. 7A and supplementary material Fig. S3). As is the case for HeLa cells, these uneven pore patterns apparently originate

Fig. 6. Ectopic expression of lamin A induces formation of the pore-free islands. Transient expression of Venus-lamin-A in HeLa cells with uniform pore distributions. Nuclear surface images of HeLa cells (Fig. 4A) expressing Venus-lamin-A and stained for nuclear pores. Enrichment of expressed Venus-lamin-A induces distinct pore-free islands (arrows).
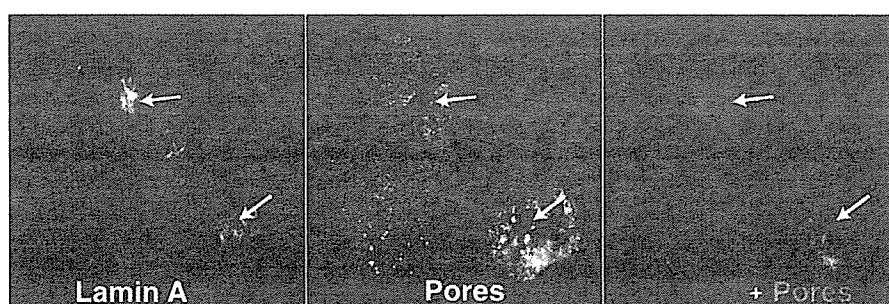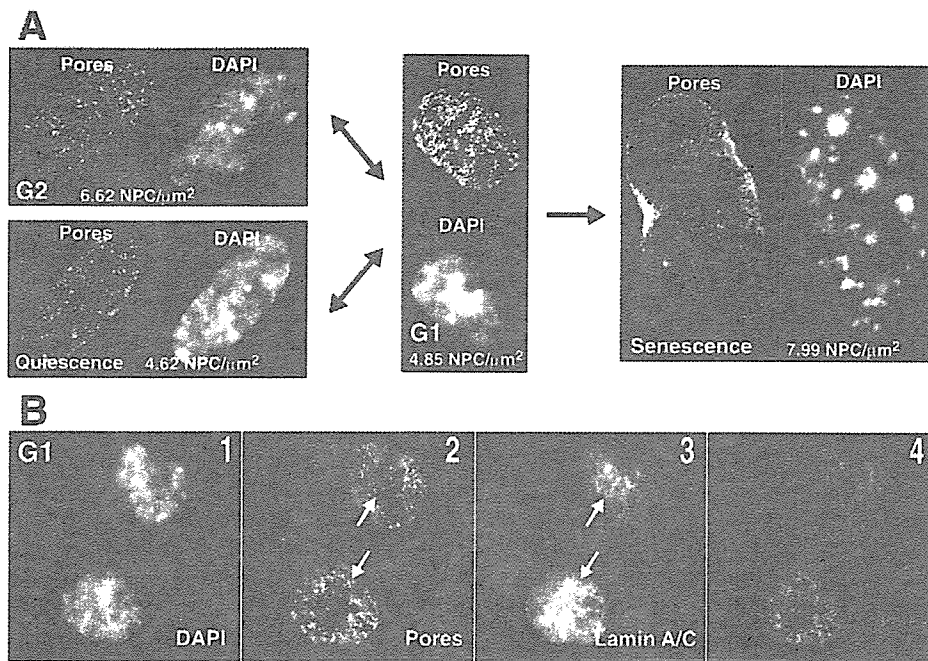
Fig. 7. Conserved structure and dynamics of pore-free islands in human normal diploid fibroblast IMR90 cells. (A) Dynamic changes in nuclear pore distributions during the cell cycle of human normal diploid IMR90 fibroblasts. In the G1 nucleus (center), the pore distribution displayed a patched pattern (see also supplementary material Fig. S3), but upon cell-cycle progression, pore distribution becomes uniform, coupled with an increase in pore number (top left). Quiescent cells induced by serum depletion still have patched pore distribution (bottom left), whereas the senescent cell nucleus shows a uniform pore distribution with a high density of pores (right). Note that DAPI staining of the senescent nucleus shows typical heterochromatic foci in the nucleoplasm (SAHF). (B) Lamin A/C is enriched in the pore-free islands of G1 nuclei of IMR90 cells (arrows), suggesting the structural conservation of the pore-free islands. 1, DAPI; 2, nuclear pores; 3, lamin A/C; 4, merged images of nuclear pores and lamin A/C.

from the beginning of telophase, when nuclear pores and lamin A/C are recruited to the surface of chromosome clusters (or mass) in a mutually exclusive manner (supplementary material Fig. S3). The pore density in early G1 is 4.85±0.40 NPCs/μm^2 (Fig. 7A). The pore distributions then become uniform in a later stage (G2), with an increase in pore density to 6.62±0.47 NPCs/μm^2, showing that such nuclear pore dynamics are ubiquitous in human cell lines.

Interestingly, in the replicative senescent state, the distribution of nuclear pores becomes much more uniform, with increased pore density to 7.99±0.18 NPCs/μm^2, whereas the distribution and density of pores in the quiescent cells (G0) by serum depletion remained very similar to those of G1 nuclei (4.62±0.44 NPCs/μm^2). The patched pattern of the uneven pore distribution is thus more prominent in the early stage of the cell cycle, and is maintained in the quiescent state (G0). Notably the patched pore pattern in the quiescent cells is easily reversed to the normal cell cycle state by serum add-back. With the progression of the cell cycle, or in the replicative senescent state, the patched pattern became dispersed, probably coupled with an increase in pore number. These findings indicate that the distribution and density of nuclear pores in the normal diploid cells significantly change during the cell-cycle progression and upon the physiological state of the cells. Moreover, lamin A/C accumulates in the pore-free islands, in the early stages of IMR90 (Fig. 7B). These results clearly show the generality of structural organization and dynamics of pore-free islands.

Discussion

Emerin, lamin A/C, and lamin B in the pore-free islands

In this study, we investigated cell-cycle-dependent dynamics of nuclear pores and found novel subdomain (island) of the nuclear envelope in human normal diploid fibroblasts IMR90 and other cell lines. The islands are devoid of nuclear pores

and enriched with inner nuclear membrane proteins emerin and lamin A/C (Figs 2-3 and supplementary material Fig. S1B,C). The siRNA-mediated knockdown of lamin A/C in the cells led to dispersal of the pore-free islands (Fig. 5A). It should be noted that the knockdown of lamin A/C did not affect the cell growth (Harborth et al., 2001) (not shown) and cell-cycle profile (Fig. 5A). By contrast, a reduction in emerin did not have a significant effect on the islands (Fig. 5B). This is not so surprising for the following reasons. Consistent with previous reports (Harborth et al., 2001; Sullivan et al., 1999), the knockdown of lamin A/C strongly enhanced an unusual cytoplasmic distribution of emerin (not shown). However, a reduction in emerin levels had no influence on the localization of lamin A/C, indicating that lamin A/C serves to immobilize emerin. Moreover, an ectopic expression of lamin A had a significant effect on the distribution of nuclear pores (Fig. 6). Lamin A/C thus plays a dominant role in the formation of the pore-free islands, possibly in cooperation with other inner nuclear membrane proteins such as lamin binding proteins (LAPs).

Interestingly, the staining of lamin B, which is a constitutively expressed B-type lamin (Harborth et al., 2001; Lenz-Bohme et al., 1997; Liu et al., 2000) and lamin B receptor (LBR), indicate that it is rarely located in the pore-free islands in HeLa S3 cells (Fig. 3B and supplementary material Fig. S2A). This suggests that A-type and B-type lamins are preferentially incorporated into rather discrete regions on the inner nuclear envelope, having a surprisingly clear correlation with the nuclear pore distribution. Several studies have reported that lamin B could be associated with the nuclear pores, through some nucleoporins (Hawryluk-Gara et al., 2005; Smythe et al., 2000). Their interaction(s) might imply a role for lamin B in recruiting and/or the spacing of nuclear pores, as obtained from genetic evidence (Lenz-Bohme et al., 1997; Liu et al., 2000). Our results also suggest a clear functional

difference, regarding pore formation, between lamin B and lamin A/C that is generally expressed in differentiated cells.

Regulation of nuclear pore distributions and density by lamin A/C

As shown in supplementary material Fig. S5C, we observed that HeLa cells with lower amounts of lamin A/C and uniform pore distribution, have a higher proliferation activity than HeLa S3 and U2-OS cells. In good agreement with our observations, embryonic cells whose nuclei lack A-type lamins have a much higher nuclear pore density (40-50 NPCs/μm^2) and proliferation activity (Maul et al., 1980). Furthermore, several studies have reported that the absence or downregulation of lamin A/C is correlated with rapid growth or aggressivity in human malignancies including small-cell lung carcinoma (Broers and Ramaekers, 1994), testicular cancer (Machiels et al., 1997), leukemias and lymphomas (Stadelmann et al., 1990) and skin carcinomas (Venables et al., 2001). These reports support the hypothesis that lamin A/C has a negative influence on cell proliferation. The suppression of lamin A/C might contribute to tumorigenesis through increasing pore density. It was recently reported that the epigenetic silencing of the lamin A/C gene by CpG island promoter hypermethylation is responsible for the loss of expression in leukemias and lymphomas (Agrelo et al., 2005). Such epigenetic effects might cause variations of lamin A/C expression in HeLa cells.

Dynamic change(s) of the pore-free islands during the cell cycle

In the present study, we show that lamin A/C plays an essential structural and regulatory role in the formation of the pore-free islands. Besides lamin A/C, what else would be involved in the event? Interestingly, many Ki-67 punctuate foci are also localized in the pore-free islands in the early G1 phase (supplementary material Fig. S4A). These foci are often accompanied by bright foci upon DAPI staining (supplementary material Fig. S4A, panels 2 and 3). Since it was shown that Ki-67 interacts with the heterochromatin protein HP1 (Kametaka et al., 2002; Scholzen et al., 2002), some pore-free islands would layer over the heterochromatic regions. Consistent with this observation, we also found that PCNA foci in the mid-to-late S phase, which are associated with the late-replicated heterochromatic regions (Dimitrova et al., 1999; O'Keefe et al., 1992), are often located in the small pore-free areas (supplementary material Fig. S4B). Such peripheral heterochromatin layers and the highly accumulated filamentous meshwork of lamin A/C might inhibit novel pore formation, creating the pore-free islands. Alternatively, this kind of stable and rigid structure might also prevent the migration of neighboring nuclear pores into the pore-free islands.

It is notable that the relationship between lamin A/C and nuclear pores is maintained throughout the cell cycle (supplementary material Fig. S1B). Accordingly, the dynamic change(s) in pore distribution described here could be triggered by a cell-cycle-specific reorganization of lamin A/C, which might be coupled with rearrangements in the heterochromatin layer beneath. In fact, it was reported that large-scale chromosomal movements indeed occur within the nuclei during the progression of G1 phase (Csink and Henikoff, 1998; Walter et al., 2003).

Of particular interest is the difference in pore distribution

between the quiescence (G0) and replicative senescence of human fibroblast IMR90 (Fig. 7A): whereas, in the quiescent cells, they remain patched pattern similar to those of G1 nuclei, the senescent cells have a much more uniform distribution, with a higher density of pores (Fig. 7A). Since both are in a 'non-dividing' state, such striking difference might reflect their distinct physiological activity or metabolism.

Physiological relevance of the pore-free islands

Why do pore-free islands exist? First, an apparent effect of the pore-free islands on the nuclear envelope is to create nuclear regions that will be deficient in nucleocytoplasmic transport. This might have drastic effects on many aspects of local nuclear functions if there are any transcription-coupled mRNA export systems, such as those proposed in yeast (Rodriguez-Navarro et al., 2004; Vinciguerra and Stutz, 2004). Indeed, inside the HeLa S3 cells, nuclei are closely surrounded with ER and Golgi apparatus spreading into the edge of the cells. The pore-free islands are, however, excluded from such organelles (supplementary material Fig. S5A), suggesting an optimal cellular architecture of HeLa S3 cells for an efficient transport system. Second, recent publications demonstrate some direct connections between nuclear pores and gene regulation, via nucleoporin and gene-promoter interactions upon transcriptional activation (Casolari et al., 2004; Ishii et al., 2002; Schmid et al., 2006). In fact, the pore-free islands comprise vast heterochromatin regions, which are normally gene silent, beneath them (supplementary material Fig. S4). Pore-rich and pore-poor subdomains on the nuclear envelope might reflect gene(s) activation and silencing states of the corresponding nuclear surface of certain chromosome territories. Indeed, levels of in vivo incorporation of BrUTP in nuclei with large pore-free islands was significantly lower than the nuclei with uniform pore distribution, suggesting a correlation between nuclear pore density and transcriptional activity (supplementary material Fig. S5B).

With the newly identified subdomain (island) of the nuclear envelope, we could also follow the dynamics of nuclei. In HeLa cells, the pore-free islands localize on both sides of the telophase nuclei (Fig. 3A). In G1 nuclei, the pore-free islands are confined on their top and bottom (Fig. 3A). This drastic change of the pore-free island positioning is considered to be a consequence of a dynamic movement of the nuclei during the early cell-cycle stages.

In conclusion, nuclear envelope subdomains, represented by lamin-A/C-enriched pore-free islands, were identified in all the human cell lines examined. Their regulation in cell cycle-dependent dynamics would be controlled by the reorganization of inner nuclear structures. Such general periodic dynamics of subdomain might reflect yet undefined nuclear functions.

Materials and Methods

Cells and antibodies

Anti-lamin A/C (SC7292), anti-lamin B (SC6216) and anti-PCNA (SC7907) antibodies were purchased from Santa Cruz Biotechnology. Anti-emerin rabbit serum was kindly provided by K. Wilson (Johns-Hopkins University, Baltimore, MD). mAb414 (ab24609) and anti-human CENP-F (ab5) antibody were obtained from Abcom. Anti-lap2β (611000), LBR (1398-1) and Ki-67 (NA59) antibodies were from BD Transduction Laboratories, Epitomics and Oncogene, respectively. Preparation of monoclonal antibody against p62, MAb 2A11, is described below. Both monoclonal antibodies, MAb 2A11 and MAb414, gave the same staining patterns of nuclear pores in all figures presented in this study.

The anti-p62 rat monoclonal antibody was generated as follows, mainly based on the rat lymph node method established by Kishiro et al. (Kishiro et al., 1995). A ten-week-old female WKY/NCrj rat (Charles River) was immunized with an emulsion containing recombinant GST-fused human p62 (1-300 aa) protein and Freund's complete adjuvant. After 3 weeks, the cells from the lymph nodes of a rat immunized with an antigen were fused with mouse myeloma Sp2/0-Ag14 cells. At 10 days post fusion, the hybridoma supernatants were screened by means of ELISA against recombinant GST-fused human p62 protein. Positive clones were subcloned and rescreened by immunoblotting and immunostaining. Finally, a monoclonal antibody, clone 2A11, was selected. The mAb 2A11 was found to be an IgG1(κ) subtype via the use of a rat antibody isotyping kit.

Immunofluorescence staining of cells

HeLaS3, HeLa, IMR90 and U-2 OS cells were grown on coverslips coated with poly-L-lysine (Wako, Japan). Immunofluorescence was carried out as described (Maeshima et al., 2005; Maeshima and Laemmli, 2003) with minor modifications. All the operations were performed at room temperature. The cells were washed in PBS and fixed with freshly prepared 2% paraformaldehyde in PBS for 15 minutes. The fixed cells were then treated with 50 mM glycine in HMK buffer (20 mM HEPES, pH 7.5, 1 mM MgCl$_2$, 100 mM KCl) for 5 minutes, rinsed with HMK (5 minutes), and permeabilized with 0.5% Triton X-100 (Calbiochem) in HMK for 5 minutes. After washing for 5 minutes with HMK, the cells were incubated with 10% normal goat serum (NGS) (Chemicom) in HMK for 30 minutes. The cells were incubated with the first antibody in HMK buffer containing 1% NGS for 1 hour. The antibody dilution rates used in this experiment were as follows: 1:400 for anti-p62, 1:5000 for Mab414, 1:2000 for emerin and laminA/C, 1:1000 dilution for lap2β, PCNA, Ki67 and CENP-F. After washing with HMK (five times for 3 minutes), the cells were incubated with 1:500-1:1000 goat Alexa Fluor 488 and/or 594 antibody (Invitrogen) in HMK buffer containing 1% NGS for 1 hour. After extensive washing with HMK (five times for 3 minutes), followed by counterstaining with 1 μg/ml DAPI (Roche), coverslips were mounted in PPDI [20 mM HEPES, pH 7.4, 1 mM MgCl$_2$, 100 mM KCl, 78% glycerol, 1 mg/ml paraphenylene diamine (Sigma)] and sealed with nail polish.

In some experiments, to visualize PCNA foci associated with DNA replication, before fixation, HeLa cells were extracted with 0.5% Triton X-100 in ice-cold CSK buffer [10 mM HEPES-KOH, pH 7.5, 300 mM sucrose, 100 mM NaCl, 3 mM MgCl$_2$, 100 nM Microcystin LR (Calbiochem) and 0.1 mM PMSF (Sigma)] for 2 minutes and washed with the same ice-cold buffer without Triton X-100 (twice for 3 minutes). Subsequent operations were carried out as described above. For the anti-lamin B antibody that did not work for the immunostaining of paraformaldehyde-fixed samples, a protocol that allows the retrieval of masked or hidden epitopes was used after fixation and permeabilization (Peranen et al., 1993).

Image stacks were recorded with a DeltaVision microscope (Applied Precision) using a step size of 0.2 μm. The objective used was an Olympus 100×/1.35 UPlanApo (Olympus). In the image stacks obtained as described above, optical sections including the nuclear surfaces that are close to the coverslips, are shown in the figures because this makes it possible to display a number of nuclear surfaces on the same focal plain. It should be noted that all the images are shown without deconvolution. The chromatic aberration in the Z-axis was corrected by shifting the different channels relative to each other as described by Maeshima and Laemmli (Maeshima and Laemmli, 2003). The measured chromatic shift was 0.4 μm between the blue and green channel and 0.6 μm between the blue and red channel. These values were obtained with the help of three-color beads of 0.1 μm diameter (Molecular Probes). The lateral chromatic aberration was measured to be negligible. To determine density of nuclear pores, the number of nuclear pores in two different areas of 25 μm^2 on each nuclear surface in five independent cells was counted and used to get average density of nuclear pores. The average density of nuclear pores is shown with standard deviation.

Scanning electron microscopy

Synchronized mitotic cells (see above) were seeded onto poly-L-lysine-coated metal specimen holders and cultured for 3 hours. The cells on the specimen holders were frozen rapidly in liquid propane (–184°C), fractured in a cryo-transfer system at –120°C (Alto-2500, Oxford, Oxon, UK). The fractured cells were coated by Cr and observed by FE-SEM (LE01530, LEO, Oberkochen, Germany).

Knockdown of laminA/C and emerin by siRNA in HeLa S3 cells

Pre-annealed dsRNAs were purchased from Qiagen. The siRNA sequences targeting

lamin A/C and emerin are as follows: lamin A/C (CUGGACUUCCAGAAGAACA-dTT based on accession number NM_005572) and emerin (CCGUGCUCC-UGGGGCUGG GdTT, based on NM_000117). siRNA transfection was carried out essentially as described by Harborth et al. (Harborth et al., 2001) with minor modifications as follows: The day before transfection, 0.3×10^5 HeLa S3 cells were seeded onto poly-L-lysine-coated coverslips in 12-well plates (2 ml per well). The transient transfection of siRNAs was carried out using Oligofectamine (GibcoBRL). 48 μl Opti-MEM1 medium (GibcoBRL) and 12 μl Oligofectamine per well were preincubated for 5-10 minutes at room temperature and 200 μl Opti-MEM 1 medium were mixed with 12 μl siRNA. The two mixtures were combined and incubated for 20 minutes at room temperature for complex formation. The entire mixture was added to the seeded cells with a final concentration of 100 nM for the siRNAs. Cells were typically assayed 48-72 hours after transfection by immunofluorescence. In some cases, to prevent the transfected cells from becoming confluent, the cells were diluted fourfold and seeded again onto coverslips 24 hours after transfection. The cell cycle profile of the lamin A/C knockdown cells was examined by Olympus LCS2 (Olympus, Japan) and shown as histograms of DNA content.

Construction of plasmid

Lamin A cDNA was amplified from a cDNA library by PCR. The cDNA library was synthesized from HeLaS3 total RNAs by Super-Script III (Invitrogen). The PCR primers used are as follows: 5'-CTGGCAACCTGCCGGCCATG-3' and 5'-GTCCCAGATTACATGATGCT-3'. Amplified fragments were cloned and sequenced for verification.

An expression clone, pEXPR-EF-1α–Venus-laminA, was constructed using the multi-site Gateway system, essentially as described previously (Sasaki et al., 2004; Yahata et al., 2005). In brief, a destination vector, pEF5/FRT/V5-DEST (Invitrogen), carrying the EF-1α promoter, was used with two entry clones, pENTR-L1-SDK-Venus (no stop)-GGSGGT-L3 and pENTR-R3r-LaminA (stop)-L2, to obtain clone encoding chimera of Venus fused at the N-terminal site of LaminA. Two entry clones, pENTR-L1-SDK-Venus (no stop)-GGSGGT-L3 and pENTR-R3r-LaminA (stop)-L2, were constructed from Venus and Lamin A cDNAs amplified from pCS2-Venus and lamin A clone (Nagai et al., 2002) (above) and donor vectors, pDONR-P1P3r (for Venus) and pDONR-P3P2 (for Lamin A), using BP reactions. Sequences of entry clones were verified using ABI PRISM® 3100 Genetic Analyzer (Applied Biosystems).

Transient expression of Venus-lamin A and Venus-p62 in HeLa cells

For transfection of the plasmid, Effectene (Qiagen) was used according to the instruction manual. For ectopic expression experiments of lamin A (Fig. 6), at 48 hours after transfection, the pore distribution on the nuclear surface was examined by the nuclear pore staining as described above.

Mathematical consideration of the pore-free islands

If the pore distributions on the nuclear surface are assumed to occur at random, and to follow a Poisson Distribution, the probability of number of nuclear pores (k) on area S (μm^2) is $P(k; \lambda S)=\exp[-\lambda S](\lambda S)^k/k!$, where λ is the expected number of occurrences, that is, the average pore density. The probability of no nuclear pores in area S is $P(0; \lambda S)=\exp[-\lambda S]$. Since a typical area of pore-free island in the G1 phase is about 30 μm^2 and average pore density in the nucleus is about 7 NPCs/μm^2, the probability of such a pore-free island occurring by chance, is about 1×10^{-79}.

References

Aebi, U., Cohn, J., Buhle, L. and Gerace, L. (1986). The nuclear lamina is a meshwork of intermediate-type filaments. *Nature* **323**, 560-564.

Agrelo, R., Setien, F., Espada, J., Artiga, M. J., Rodriguez, M., Perez-Rosado, A., Sanchez-Aguilera, A., Fraga, M. F., Piris, M. A. and Esteller, M. (2005). Inactivation of the lamin A/C gene by CpG island promoter hypermethylation in

hematologic malignancies, and its association with poor survival in nodal diffuse large B-cell lymphoma. *J. Clin. Oncol.* **23**, 3940-3947.

Broers, J. L. and Ramaekers, F. C. (1994). Differentiation markers for lung-cancer sub-types. A comparative study of their expression in vivo and in vitro. *Int. J. Cancer Suppl.* **8**, 134-137.

Burke, B. and Stewart, C. L. (2002). Life at the edge: the nuclear envelope and human disease. *Nat. Rev. Mol. Cell Biol.* **3**, 575-585.

Casolari, J. M., Brown, C. R., Komili, S., West, J., Hieronymus, H. and Silver, P. A. (2004). Genome-wide localization of the nuclear transport machinery couples transcriptional status and nuclear organization. *Cell* **117**, 427-439.

Cronshaw, J. M., Krutchinsky, A. N., Zhang, W., Chait, B. T. and Matunis, M. J. (2002). Proteomic analysis of the mammalian nuclear pore complex. *J. Cell Biol.* **158**, 915-927.

Csink, A. K. and Henikoff, S. (1998). Large-scale chromosomal movements during interphase progression in Drosophila. *J. Cell Biol.* **143**, 13-22.

Daigle, N., Beaudouin, J., Hartnell, L., Imreh, G., Hallberg, E., Lippincott-Schwartz, J. and Ellenberg, J. (2001). Nuclear pore complexes form immobile networks and have a very low turnover in live mammalian cells. *J. Cell Biol.* **154**, 71-84.

Davis, L. I. (1995). The nuclear pore complex. *Annu. Rev. Biochem.* **64**, 865-896.

Dimitrova, D. S., Todorov, I. T., Melendy, T. and Gilbert, D. M. (1999). Mcm2, but not RPA, is a component of the mammalian early G1-phase prereplication complex. *J. Cell Biol.* **146**, 709-722.

Elbashir, S. M., Harborth, J., Lendeckel, W., Yalcin, A., Weber, K. and Tuschl, T. (2001). Duplexes of 21-nucleotide RNAs mediate RNA interference in cultured mammalian cells. *Nature* **411**, 494-498.

Fahrenkrog, B., Koser, J. and Aebi, U. (2004). The nuclear pore complex: a jack of all trades? *Trends Biochem. Sci.* **29**, 175-182.

Gerace, L. and Burke, B. (1988). Functional organization of the nuclear envelope. *Annu. Rev. Cell Biol.* **4**, 335-374.

Goldman, R. D., Gruenbaum, Y., Moir, R. D., Shumaker, D. K. and Spann, T. P. (2002). Nuclear lamins: building blocks of nuclear architecture. *Genes Dev.* **16**, 533-547.

Gorlich, D. and Kutay, U. (1999). Transport between the cell nucleus and the cytoplasm. *Annu. Rev. Cell Dev. Biol.* **15**, 607-660.

Haraguchi, T., Koujin, T., Hayakawa, T., Kaneda, T., Tsutsumi, C., Imamoto, N., Akazawa, C., Sukegawa, J., Yoneda, Y. and Hiraoka, Y. (2000). Live fluorescence imaging reveals early recruitment of emerin, LBR, RanBP2, and Nup153 to reforming functional nuclear envelopes. *J. Cell Sci.* **113**, 779-794.

Haraguchi, T., Koujin, T., Segura-Totten, M., Lee, K. K., Matsuoka, Y., Yoneda, Y., Wilson, K. L. and Hiraoka, Y. (2001). BAF is required for emerin assembly into the reforming nuclear envelope. *J. Cell Sci.* **114**, 4575-4585.

Harborth, J., Elbashir, S. M., Bechert, K., Tuschl, T. and Weber, K. (2001). Identification of essential genes in cultured mammalian cells using small interfering RNAs. *J. Cell Sci.* **114**, 4557-4565.

Hawryluk-Gara, L. A., Shibuya, E. K. and Wozniak, R. W. (2005). Vertebrate Nup53 interacts with the nuclear lamina and is required for the assembly of a Nup93-containing complex. *Mol. Biol. Cell* **16**, 2382-2394.

Hetzer, M. W., Walther, T. C. and Mattaj, I. W. (2005). Pushing the envelope: structure, function, and dynamics of the nuclear periphery. *Annu. Rev. Cell Dev. Biol.* **21**, 347-380.

Hutchison, C. J. and Worman, H. J. (2004). A-type lamins: guardians of the soma? *Nat. Cell Biol.* **6**, 1062-1067.

Hutchison, C. J., Alvarez-Reyes, M. and Vaughan, O. A. (2001). Lamins in disease: why do ubiquitously expressed nuclear envelope proteins give rise to tissue-specific disease phenotypes? *J. Cell Sci.* **114**, 9-19.

Imamoto, N. (2000). Diversity in nucleocytoplasmic transport pathways. *Cell Struct. Funct.* **25**, 207-216.

Ishii, K., Arib, G., Lin, C., Van Houwe, G. and Laemmli, U. K. (2002). Chromatin boundaries in budding yeast: the nuclear pore connection. *Cell* **109**, 551-562.

Kametaka, A., Takagi, M., Hayakawa, T., Haraguchi, T., Hiraoka, Y. and Yoneda, Y. (2002). Interaction of the chromatin compaction-inducing domain (LR domain) of Ki-67 antigen with HP1 proteins. *Genes Cells* **7**, 1231-1242.

Kill, I. R. (1996). Localisation of the Ki-67 antigen within the nucleolus. Evidence for a fibrillarin-deficient region of the dense fibrillar component. *J. Cell Sci.* **109**, 1253-1263.

Kishiro, Y., Kagawa, M., Naito, I. and Sado, Y. (1995). A novel method of preparing rat-monoclonal antibody-producing hybridomas by using rat medial iliac lymph node cells. *Cell Struct. Funct.* **20**, 151-156.

Kubitscheck, U., Wedekind, P., Zeidler, O., Grote, M. and Peters, R. (1996). Single nuclear pores visualized by confocal microscopy and image processing. *Biophys. J.* **70**, 2067-2077.

Lenz-Bohme, B., Wismar, J., Fuchs, S., Reifegerste, R., Buchner, E., Betz, H. and Schmitt, B. (1997). Insertional mutation of the Drosophila nuclear lamin Dm0 gene results in defective nuclear envelopes, clustering of nuclear pore complexes, and accumulation of annulate lamellae. *J. Cell Biol.* **137**, 1001-1016.

Liao, H., Winkfein, R. J., Mack, G., Rattner, J. B. and Yen, T. J. (1995). CENP-F is a protein of the nuclear matrix that assembles onto kinetochores at late G2 and is rapidly degraded after mitosis. *J. Cell Biol.* **130**, 507-518.

Liu, J., Rolef Ben-Shahar, T., Riemer, D., Treinin, M., Spann, P., Weber, K., Fire, A. and Gruenbaum, Y. (2000). Essential roles for Caenorhabditis elegans lamin gene in nuclear organization, cell cycle progression, and spatial organization of nuclear pore complexes. *Mol. Biol. Cell* **11**, 3937-3947.

Macara, I. G. (2001). Transport into and out of the nucleus. *Microbiol. Mol. Biol. Rev.* **65**, 570-594.

Machiels, B. M., Ramaekers, F. C., Kuijpers, H. J., Groenewoud, J. S., Oosterhuis, J. W. and Looijenga, L. H. (1997). Nuclear lamin expression in normal testis and testicular germ cell tumours of adolescents and adults. *J. Pathol.* **182**, 197-204.

Maeshima, K. and Laemmli, U. K. (2003). A two-step scaffolding model for mitotic chromosome assembly. *Dev. Cell* **4**, 467-480.

Maeshima, K., Eltsov, M. and Laemmli, U. K. (2005). Chromosome structure: improved immunolabeling for electron microscopy. *Chromosoma* **114**, 365-375.

Maul, G. G., Price, J. W. and Lieberman, M. W. (1971). Formation and distribution of nuclear pore complexes in interphase. *J. Cell Biol.* **51**, 405-418.

Maul, G. G., Deaven, L. L., Freed, J. J., Campbell, G. L. and Becak, W. (1980). Investigation of the determinants of nuclear pore number. *Cytogenet. Cell Genet.* **26**, 175-190.

Mounkes, L., Kozlov, S., Burke, B. and Stewart, C. L. (2003). The laminopathies: nuclear structure meets disease. *Curr. Opin. Genet. Dev.* **13**, 223-230.

Nagai, T., Ibata, K., Park, E. S., Kubota, M., Mikoshiba, K. and Miyawaki, A. (2002). A variant of yellow fluorescent protein with fast and efficient maturation for cell-biological applications. *Nat. Biotechnol.* **20**, 87-90.

O'Keefe, R. T., Henderson, S. C. and Spector, D. L. (1992). Dynamic organization of DNA replication in mammalian cell nuclei: spatially and temporally defined replication of chromosome-specific alpha-satellite DNA sequences. *J. Cell Biol.* **116**, 1095-1110.

Oberleithner, H., Brinckmann, E., Schwab, A. and Krohne, G. (1994). Imaging nuclear pores of aldosterone-sensitive kidney cells by atomic force microscopy. *Proc. Natl. Acad. Sci. USA* **91**, 9784-9788.

Peranen, J., Rikkonen, M. and Kaariainen, L. (1993). A method for exposing hidden antigenic sites in paraformaldehyde-fixed cultured cells, applied to initially unreactive antibodies. *J. Histochem. Cytochem.* **41**, 447-454.

Rabut, G., Doye, V. and Ellenberg, J. (2004). Mapping the dynamic organization of the nuclear pore complex inside single living cells. *Nat. Cell Biol.* **6**, 1114-1121.

Rodriguez-Navarro, S., Fischer, T., Luo, M. J., Antunez, O., Brettschneider, S., Lechner, J., Perez-Ortin, J. E., Reed, R. and Hurt, E. (2004). Sus1, a functional component of the SAGA histone acetylase complex and the nuclear pore-associated mRNA export machinery. *Cell* **116**, 75-86.

Rout, M. P. and Wente, S. R. (1994). Pores for thought: nuclear pore complex proteins. *Trends Cell Biol.* **4**, 357-365.

Rout, M. P., Aitchison, J. D., Suprapto, A., Hjertaas, K., Zhao, Y. and Chait, B. T. (2000). The yeast nuclear pore complex: composition, architecture, and transport mechanism. *J. Cell Biol.* **148**, 635-651.

Sasaki, Y., Sone, T., Yoshida, S., Yahata, K., Hotta, J., Chesnut, J. D., Honda, T. and Imamoto, F. (2004). Evidence for high specificity and efficiency of multiple recombination signals in mixed DNA cloning by the Multisite Gateway system. *J. Biotechnol.* **107**, 233-243.

Schmid, M., Arib, G., Laemmli, C., Nishikawa, J., Durussel, T. and Laemmli, U. K. (2006). Nup-PI: the nucleopore-promoter interaction of genes in yeast. *Mol. Cell* **21**, 379-391.

Scholzen, T., Endl, E., Wohlenberg, C., van der Sar, S., Cowell, I. G., Gerdes, J. and Singh, P. B. (2002). The Ki-67 protein interacts with members of the heterochromatin protein 1 (HP1) family: a potential role in the regulation of higher-order chromatin structure. *J. Pathol.* **196**, 135-144.

Smythe, C., Jenkins, H. E. and Hutchison, C. J. (2000). Incorporation of the nuclear pore basket protein nup153 into nuclear pore structures is dependent upon lamina assembly: evidence from cell-free extracts of Xenopus eggs. *EMBO J.* **19**, 3918-3931.

Stadelmann, B., Khandjian, E., Hirt, A., Luthy, A., Weil, R. and Wagner, H. P. (1990). Repression of nuclear lamin A and C gene expression in human acute lymphoblastic leukemia and non-Hodgkin's lymphoma cells. *Leuk. Res.* **14**, 815-821.

Stuurman, N., Heins, S. and Aebi, U. (1998). Nuclear lamins: their structure, assembly, and interactions. *J. Struct. Biol.* **122**, 42-66.

Sullivan, T., Escalante-Alcalde, D., Bhatt, H., Anver, M., Bhat, N., Nagashima, K., Stewart, C. L. and Burke, B. (1999). Loss of A-type lamin expression compromises nuclear envelope integrity leading to muscular dystrophy. *J. Cell Biol.* **147**, 913-920.

Suntharalingam, M. and Wente, S. R. (2003). Peering through the pore: nuclear pore complex structure, assembly, and function. *Dev. Cell* **4**, 775-789.

Vasu, S. K. and Forbes, D. J. (2001). Nuclear pores and nuclear assembly. *Curr. Opin. Cell Biol.* **13**, 363-375.

Venables, R. S., McLean, S., Luny, D., Moteleb, E., Morley, S., Quinlan, R. A., Lane, E. B. and Hutchison, C. J. (2001). Expression of individual lamins in basal cell carcinomas of the skin. **84**, 512-519.

Vinciguerra, P. and Stutz, F. (2004). mRNA export: an assembly line from genes to nuclear pores. *Curr. Opin. Cell Biol.* **16**, 285-292.

Walter, J., Schermelleh, L., Cremer, M., Tashiro, S. and Cremer, T. (2003). Chromosome order in HeLa cells changes during mitosis and early G1, but is stably maintained during subsequent interphase stages. *J. Cell Biol.* **160**, 685-697.

Wilson, K. L. (2000). The nuclear envelope, muscular dystrophy and gene expression. *Trends Cell Biol.* **10**, 125-129.

Yahata, K., Kishine, H., Sone, T., Sasaki, Y., Hotta, J., Chesnut, J. D., Okabe, M. and Imamoto, F. (2005). Multi-gene gateway clone design for expression of multiple heterologous genes in living cells: conditional gene expression at near physiological levels. *J. Biotechnol.* **118**, 123-134.

染色体の構造とその凝縮メカニズム

前島一博

別 刷

特集　クロマチン動態による染色体制御

染色体の構造とその凝縮メカニズム
Mitotic Chromosomes : Structure and Condensation Mechanism

前島一博
Kazuhiro Maeshima

染色体は,細胞が分裂する際,複製されたゲノムの遺伝情報を2つの娘細胞に正確に分配するために必須な構造体である.長さが合計2mにも及ぶヒトゲノムDNAをわずか数μmの40数本の染色体に短時間に束ねるメカニズムは,まさに驚異的と言える.この10年間,染色体凝縮に必須なコンデンシンの発見など染色体研究に著しい進歩があった.本稿では,染色体の構造とその凝縮メカニズムについて,歴史的な背景も含めて解説したい.

key words
細胞周期, 分裂期染色体, Scaffold, コンデンシン, Topo II

[i] 前島一博　理化学研究所 中央研究所 今本細胞核機能研究室　E-mail：maeshima@riken.jp
1999年大阪大学大学院医学研究科博士課程修了,1999年から2004年までスイスジュネーブ大学分子生物学科Laemmli教授研究室で博士研究員.2005年より現所属,研究員.

はじめに

　染色体 "chromosome" は,もともとギリシャ語で "color body" を意味する言葉に由来し,文字通り細胞内で非常によく染色される構造体である.このため,古くから生物学者たちの興味を集めていた.ヒトの場合,細胞核の中に納められているDNAの長さは染色体1本あたり,数cmにも及ぶ.このため,複製された長いDNAを2つの細胞に分配するためには,DNAを1万倍以上にコンパクトに凝縮させなければならない.それでは,染色体は1本の長いDNAからいったいどのようにして構築されるのだろうか?

I.染色体の基本構造：ヌクレオソームと30nmクロマチンファイバー

　細胞の分子生物学 第4版[1]の230ページを開けてみると,図1Aのような図が載っている.まず,直径2nmのDNAから始まり,このDNAが塩基性タンパク質であるヒストンH2A, H2B, H3, H4から成る八量体に巻かれて,ヌクレオソームと呼ばれる直径約10nmの構造体ができる.このヌクレオソームの構造は図1Bのように1.9Åの精度で正確にわかっている.さらに,高次な構造体として,ヌクレオソームがリンカーヒストンであるH1を伴い,折り畳まれて直径約30nmのクロマチンファイバーになるとされている.この30nmのクロマチンファイバーは,最近までヌクレオソームが"らせん状"に折り畳まれていると考えられていたので,"ソレノイドファイバー"とも言われていた.しかしながら最近の解析の結果では,古典的なソレノイドではなく,図

1Aにあるようなジグザグ構造ではないかと示唆されているが,いまだ正確にはわかっていない.さらに,このクロマチンファイバーがどのようにして,最終的に直径約1μmの分裂期染色体を作るのかについてはいまだまったくの謎である.これからこの謎に対して,どのようなアプローチがなされてきたか,少し振り返ってみたい.

II.ヒストンリン酸化

　染色体は1/3がヒストンタンパク質からできている.このため,何が分裂期染色体の凝縮を担っているかを考えたとき,最初に注目されたのは染色体中のヒストン修飾であった.実際,1970年代後半,ヒストンH1とH3のリン酸化が見つかった[2].H2Aのリン酸化やH2B, H3, H4のアセチル化は細胞周期を通じてほぼ一定であるのに対し,H1のリン酸化はS期,G2期と上昇し,M期にピークに達する.H3のリン酸化に至っては,ほとんどM期特異的に起こっていることが観察された[2].H1のリン酸化部位は数カ所存在し,H3はテール(図1B)にある10番目のセリンである(後に28番目のセリンのリン酸化も見つかった).このため,長い間これらのヒストンの分裂期特異的なリン酸化が,染色体の凝縮を担っていると考えられてきた.しかしながら,アフリカツメガエルの卵細胞抽出液(詳しくは文献3のコラム参照)や,哺乳類の系では,H3のリン酸化を引き起こすAurora Bキナーゼなしでも染色体凝縮自体は問題なく起こる[4].H1に関しても,染色体凝縮には関与してないという証拠がいくつか提示されている.では,ヒストンでなければどのようなタンパク質が染色体凝縮に関わっているのだろうか?